Study of Automatic Segmentation and Boundary Curve Methods for Heart sound Analysis and VSD Diagnosis

Shuping Sun

Yamaguchi University

JULY 2013

A thesis submitted for the degree of doctor

The Graduate School of Science and Engineering

Yamaguchi University

Abstract

Congenital heart defects are abnormalities in the heart's structure that are present at birth. Approximately 8 out of every 1,000 newborns have congenital heart defects, which can range from mild to severe. If it is diagnosed in early stage, there will be more treatment options available for congenital heart defects and the most defects could be cured successfully. A ventricular septal defect (VSD), one of the most common congenital heart defects and accounting for 30% of all congenital heart defects, presents a hole in the septum of the ventricles. According to the sizes of the hole, clinically, a VSD is generally classified into three types: SVSD (the defect diameter is smaller than 5 mm), MVSD (the diameter is greater than 5 and smaller than 15 mm) and LVSD (the diameter is greater than 15 mm). As for the different types of VSD, the treatments are very different. Therefore, if the different types of VSD could be recognized or diagnosed with a relative high accuracy by heart sound analysis, it could be more convenient to the patients with a VSD.

In order to diagnose VSD efficiently based on heart sound analysis, the accuracy to extract the heart sound feature parameters is very important. The feature parameters in time domain and frequency domain proposed in our previous studies have been proven to be efficient for diagnosing some heart diseases. However, since the waveforms of VSD sound are too complicated and the feature parameters are very difficult to be extracted automatically. How to segment the heart sounds and to extract the feature parameters automatically and precisely is an important topic in heart sound analysis. In this study, a novel automatic algorithm for segmentation of heart sounds and the

extraction of the feature parameters is proposed first. By this algorithm the accuracies of the heart sounds segmentation and feature parameters extraction have been achieved up to 97.6%.

To diagnose the types of VSD defects based on these heart sound feature parameters, a widely used method, Support Vector Machine classifying method, has been introduced to generate the boundary curves surrounding the features datasets of the different types of VSD. In this case, the cross-over areas between the feature datasets induce the difficulty to obtain high accuracy boundary curve. In this study, a boundary curve algorithm based on support vector machines (SVM), is proposed based on the following improvements:

1. A reference dataset has been introduced for calculation of the boundary curve. The idea to generate the reference dataset is to consider the probability of the distribution of a given dataset which is to be classified.
2. The boundary curve surrounding the given dataset is solved by iterative calculation method with a kernel function of the variable parameter until it is reached to the satisfied classification accuracy.

Based on the proposed boundary curve method, the classification accuracies have been achieved to 94.8%C93.7% and 94.1% each for SVSD, MVSD and LVSD. However, the classification by the boundary curves obtained directly by the SVM method is not easy to be used in classification automatically by the computer. Especially this method does not satisfy the clinical application or household application if a tablet PC or smart phone is used. To solve this problem, in the final part of this dissertation, an ellipse model is presented to classify the VSD. The ellipse function parameters are obtained by the curve fitting method which is applied to the boundary curve obtained by SVM method. Based on the ellipse function parameters, a simple classification system is proposed for diagnosing the different types

of VSD. The classification accuracies achieved for diagnosing SVSD, MVSD and LVSD are 95.7%C94.7% and 95.0% respectively, which is almost similar to the results achieved by the SVM boundary curve method. Finally several clinical heart sound data, which are included the different sizes of VSD, normal heart sounds, aortic regurgitation (AR), atrical fibrillation (AF), aortic stenosis (AS) and mitral stenosis (MS) sounds, are used to validate the usefulness of the proposed ellipse model classification system.

Contents

Chapter 1

Introduction

1.1 Background

A ventricular septal defect (VSD) is a type of congenital heart disease (CHD) [1; 2; 3]. A VSD is a hole in the part of the septum that separates the ventricles. The hole allows oxygen-rich blood to flow from the left ventricle into the right ventricle, instead of flowing into the aorta and out to the body as it should [4; 5; 6; 7; 8; 9]. the Cross-Section of a normal heart and a heart with a VSD are shown in Figure 1.1. Figure 1.1(A) shows the structure and blood flow inside a normal heart. Figure 1.1(B) shows two common locations for a ventricular septal defect. The defect allows oxygen-rich blood from the left ventricle to mix with oxygen-poor blood in the right ventricle. In the normal heart, the septum prevents blood from flowing directly from one ventricle to the other.

It is estimated that approximately 8 in 1,000 newborns have CHD [10] which mainly includes 3 kinds of heart disease (aortic septal defect (ASD), Tetralogy of Fallot (TOF) and VSD). Figure 1.2 shows the occupancies of three kinds of heart disease. From the Figure 1.2, A VSD is the most frequent of the various types of

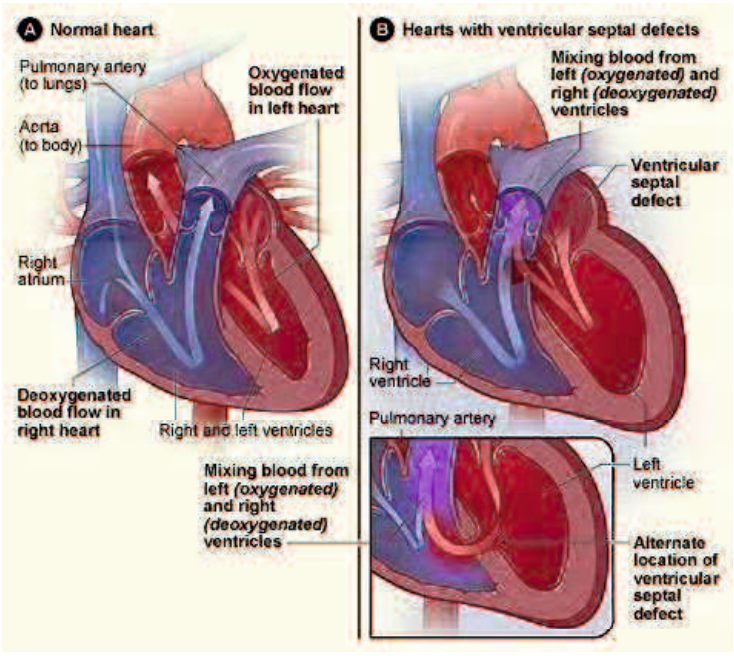

Figure 1.1 Cross-Section of a normal heart and a heart with a ventricular septal defect.

CHD (30% of all CHD) [4; 7; 11]. Approximately one infant in 1250 will be born with 3 VSD.

Based on the size of the defect [4], small VSD (named SVSD) whose defect diameter is smaller than 5 mm (denoted as $\Phi \leq 5$ mm), moderate VSD (MVSD) ($15 \geq \Phi > 5$ mm) and large VSD (LVSD)($\Phi > 15$ mm) are classified by doctor. In patients with a SVSD, there is minimal shunting of blood and the pressure in the right ventricle remains normal. Since the right ventricular pressure is normal, there is no damage to the lung arterioles. A prominent murmur along the left sterna bored heard through a stethoscope is usually the only sign that brings the VSD to attention. Children with SVSD appear healthy, and have no growth retardation. One-third to one-half of all SVSDs close spontaneously. This seemingly miraculous event occurs most often before the baby is 1 year old, almost

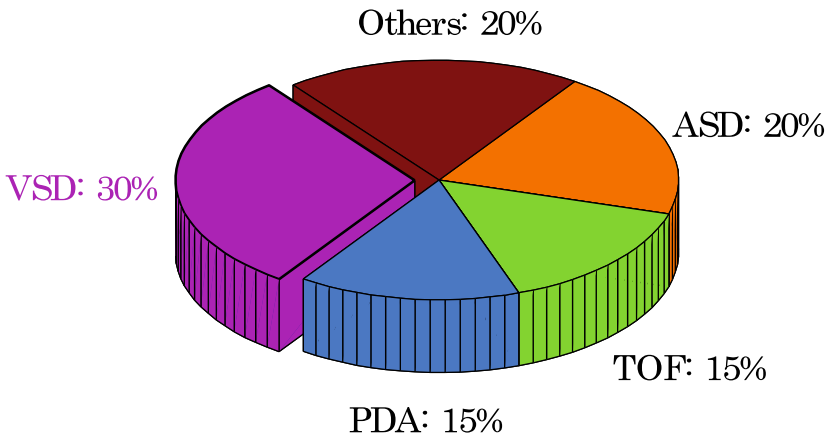

Figure 1.2 The distribution of the occupancies for three kinds of heart disease.

always before age 4 (75% by 2 years of age). Even if a SVSD does not close spontaneously, surgical repair is usually not recommended. However, long-term follow-up is required. Children with a MVSD, the shunting of blood from the left ventricle into the right ventricle is still restrictive. Therefore, pulmonary pressures may be normal or mildly elevated, but it will cause insufficient oxygenation of the blood and possibly left heart failure. The patient with MVSD may be underweight. Child with a LVSD, there is significant shunting of blood from the left ventricle through the right ventricle to the lungs and back to the left atrium and on to the left ventricle. This causes the left atrium and left ventricle to handle an increased amount of blood, and the workload on the heart increases. The increased workload on the heart also increases the heart rate and cause congestive heart failure, growth failure, bacterial endocarditis, irregular heartbeat or rhythm, Pulmonary artery hypertension, ect; ultimately, the patient with a LVSD will need surgery to "patch the hole" in the ventricular septum.

The general methods for diagnosing heart disease include chest x-ray, echocardiography, ECG, clinical auscultation, and so on. Among these methods, the heart auscultation by using stethoscope is the simplest way, and is routinely used as an early diagnostic study. According to the different sizes of VSD, the treatments are very different. Therefore, if the different sizes of VSD could be recognized or diagnosed with a gratifyingly high accuracy using heart sound analysis which is the simplest and cheapest method to noninvasively diagnose heart diseases, it will lessen the psychological and economic burden on the patients with a VSD

1.2 Review of heart sound analysis

In recent years, many researchers proposed some automatic methods for distinguishing heart sound signal by using computer technique and digital signal processing technology. No matter which methods they can be summarized by two-steps: (1) how to extract the HSs analysis features using various signal processing methods, (2) how to classify the heart disease from HSs. As for HSs analysis methods, they can be generally divided into two approaches: the time domain analysis and the frequency domain analysis.

In the time domain, since every cardiac cycle is usually composed of S1 and S2, the emphasis is how to use them to analyze HSs. These analysis methods [12; 13; 14; 15; 16; 17] can be divided into two branches. One is using the features extracted from the characteristic waveform based on S1 and S2 to analyze HSs. Furthermore, in the study [17], the diagnostic features [T11, T12, T1, T2] in the time domain extracted from the characteristic waveform have proven to be useful

for identification of normal sounds and heart diseases, including atrial fibrillation (AF), aortic regurgitation (AR) and mitral stenosis (MS); where T11 is the time interval of two adjacent S1, T12 is the time intervals between S1 and S2, T1 is the time width of S1, and T2 is the time width of S2. The other is using the segment between S1 and S2 to determine the time intervals of the systole and diastole used to analyze HSs. Moveover, the researcher [18] proposed a novel characteristic waveform (CW) for heart sounds based on the Viola integral method, which can be calculated in real time and does not require any preprocessing to reduce the effect of noise in fast algorithm.

In the frequency domain, many researches [16; 19; 20; 21; 22; 23; 24; 25; 26; 27; 28; 29; 30] have been concerning on the characteristic extraction by local frequency analysis method. In the spectral analysis, short-time Fourier transform (STFT) [19; 20; 21; 22], the wavelet decomposition or wavelet packet decomposition [22; 23; 24] are commonly used. However, in our previous study [31], using two diagnostic features [Fmax, Fwidth] to detect heart murmurs has been verified as an efficient method because the highest classification accuracies were achieved for classifying normal and abnormal HSs. Fmax describes the maximum peak of the characteristic waveform and Fwidth is the frequency width between the crossed points of the characteristic waveform on a selected threshold value. However, it is pity that there was not detail explain about how to select about one cardiac cycles heart sound signal.

As for the classifier of the heart sounds,in the meanwhile,the artificial neural network (ANN) was a computational tool for pattern classification which has been the subject of researchersf interests in the past years. For the classification of cardiac sounds, ANN or NN provided the high classification rate and

was frequently used as a classifier [19; 20; 21; 22; 22; 23; 24]. Recently,the support vector machines(SVM) proposed by Vapnik [32; 33] is a new classification technique, SVM have been used successfully for the solution of many problems including heart murmurs classification [31], cancer diagnosis [34], handwritten digital recognition [35], etc. When using SVM and selecting the radio basis function (RBF) as kernel function, the problems, how to optimal input features C , which control the tradeoff between complexity of the machine and the number of no separable points, and how to set the best kernel parameter, the width of RBF, are confronted. In the study [34], the proposed grid search approach is verified as an efficient way for searching the parameters.

However, because the mathematical expressions of the classification curves were too complicated to be expressed by parameters. Furthermore, the computation was so huge. To simplify the mathematical expressions of the classification curves to reduce the computation, based on the shapes of the classification boundary curves, the models for the classification boundary curves are considered. In order to discriminate the heart sound and reduce the discrimination error produced by observation, the numerical diagnosis system based on the numerical diagnosis results is carried out to identify VSD and different sizes, SVSD, MVSD, and LVSD. The performance of the proposed method is evaluated by clinical heart sounds.

1.3 Aim of this thesis

This thesis focuses on the development of VSD diagnostic system. In particular, the work focus on three points. First, the diagnostic features, which were the

critical factors for ensuring the success of heart disease diagnosis system, were extracted from the heart sound in the time domain and the frequency domain. Second, boundary curves based on support vector machines (SVM), which was used successfully for many problems including heart murmurs classification, cancer diagnosis, etc, was proposed to surround a given datasets and to be used as classifier to diagnose VSD. Finally, the ellipse models based on the least squares method was built to propose a high-efficient numerical diagnostic system for diagnosing the different sizes of VSD, SVSD, MVSD, and LVSD. This study includes signal processing methods, machine learning method, and classification boundary modeling procedure.

Chapter 2

HSs acquisition and pre-processing procedure

2.1 HSs acquisition

Auscultation denotes the act of analyzing sounds in the body that is produced in response to mechanical vibrations generated in the organs. The heart sounds can be collected by an electrical stethoscope. In general there are 4 positions shown in Figure 2.1, which are aortic area, pulmonary area, tricuspid area and mitral area, respectively. As for VSD cases, HSs collected from tricuspid area are reported to supply more important information [36; 37]. In this study, the HSs were all collected from tricuspid area.

For every cardiac sound cycle, there are two primary components, S1 and S2, which are generated at the end of atria contraction and the closure of the aortic valve and pulmonary valve respectively. The original heart sound is denoted here by S_{T} in the time domain and its FFT result is denoted as S_{F}.

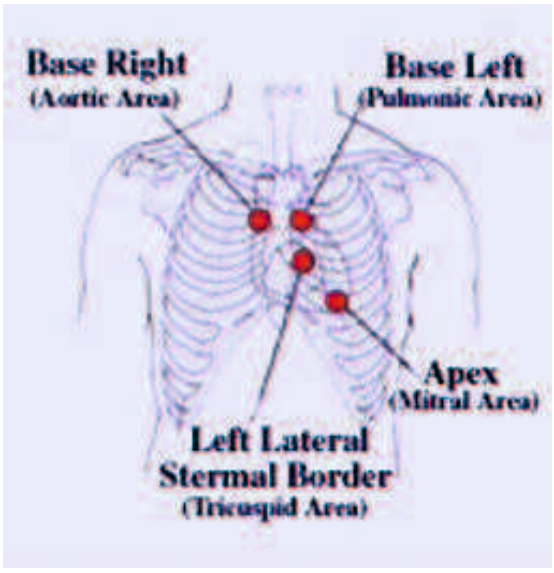

Figure 2.1 The auscultation areas for heart sounds

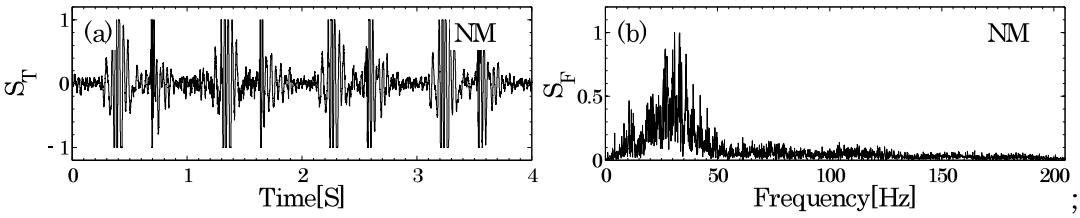

Figure 2.2 Examples for NM sounds. (a) a typical NM sounds in the time domain and (b) its Fourier transform results.

For normal sounds, the frequency distribution generally concentrate on the low frequency region and the heart beat generally 50-70 beats/ min. The typical normal sounds are named NM plotted in Figure 2.2. Figure 2.2(a) shows the plot of a normal sound in the time domain, which is a sample from a 24 years young healthy man with the heart beat of 68 beats/ min. Figure 2.2(b) is the the frequency domain results, where the peak frequency are approximately $30-50$ Hz.

For VSD sounds, in patients with a SVSD, there is minimal shunting of blood

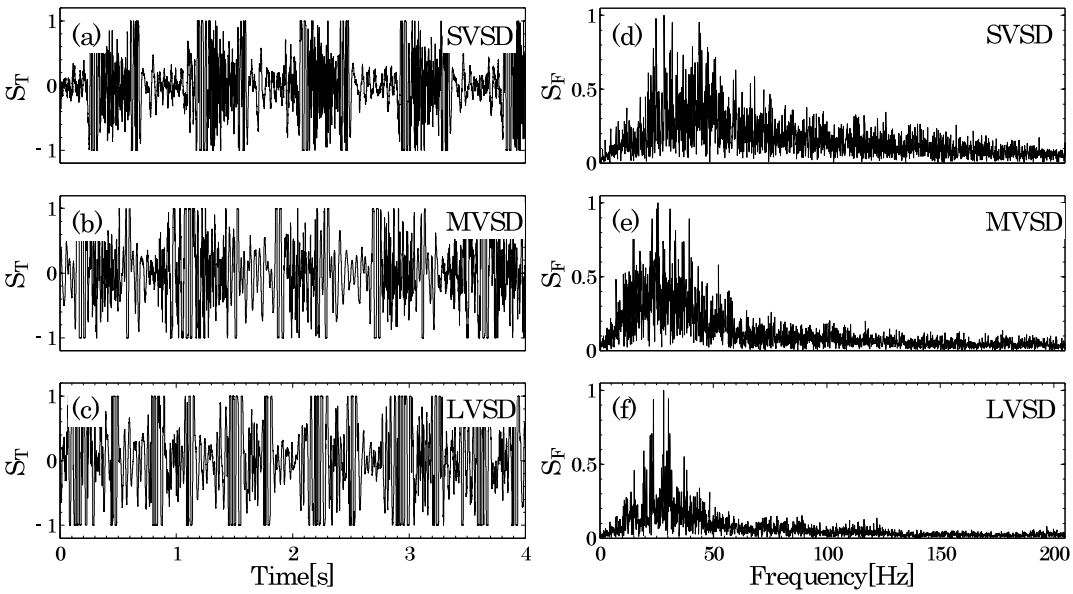

Figure 2.3 Examples for VSD sounds. (a), (b) and (c) 3 typical VSD sounds in the time domain, (d), (e) and (f) their Fourier transform results.

and the pressure in the right ventricle remains normal. Since the right ventricular pressure is normal, there is no damage to the lung arterioles and the sound is similar to the normal sounds. A typical SVSD sound extracted from a female (Φ = 4 mm, age 3, weight 30 kg, and heart beat 85 beats/min) is plotted in Figure 2.3(a) and its FFT results is plotted in Figure 2.3(d). In patients with a MVSD, the shunting of blood from the left ventricle into the right ventricle is still restrictive. Therefore, it causes insufficient oxygenation of the blood and possibly left heart failure and heart beat fast on certain degree. A typical MVSD sound extracted from the patients with MVSD (Φ = 10 mm) (a female of age 3 with weight 5 kg and 94 beats/ min heart beat) is plotted in Figure 2.3(b) and its FFT results is plotted in Figure 2.3(e). In patients with a LVSD, there is significant shunting of blood from the left ventricle through the right ventricle to the lungs and back to the left atrium and on to the left ventricle, which causes

the left atrium and left ventricle to handle an increased amount of blood, and the workload on the heart increases. The increased workload on the heart also increases the heart rate. A typical LVSD sound extracted from a female ($\Phi = 18$ mm, age 5, weight 15 kg, and heart beat 124 beats/ min) is plotted in Figure 2.3(c) and its FFT results is plotted in Figure 2.3(f). Figure 2.3 shows the fact, that is, although the heart beats is getting faster with the size of VSD increasing (Figure 2.3(a), (b) and (c)), the frequency distribution is getting narrower. Therefore, time domain analysis combined with frequency analysis might have the better performance.

2.2 Wavelet-based pre-processing procedure

The cardiac sound usually included an enormous volume of the unwanted components caused by the environmental noises, power interference, breath sound, lung sound and etc. For reasons of the complex and highly non-stationary nature of cardiac sound signals and their frequency characteristics, an appropriate pre-processing manner for noise cancellation is demanded firstly to identify the cardiac sounds effectively. Regarding this consideration, we used the wavelet decomposition (WD) as the pre-processing for the identification of cardiac sounds [38]. The wavelet transform has received attention in recent years in the analysis of non-stationary signals. The main advantage of wavelet transform is that it has a varying window size in which the wide one is good for slow frequency component and the narrow one for high frequency. Hence it provides good resolution in both time and frequency domains. In many medical applications, the wavelet transform has become a powerful alternative to FFT [22; 23; 24; 39; 40; 41; 42; 43; 44].

For the wavelet expansion [45; 46; 47; 48], a signal S_T can be described by a set of scaling functions $\varphi(t)$ and wavelet functions $\psi(t)$ that can span by various scales of the scaling function as follows:

$$S_T = \sum_{j=-\infty} c_j \varphi_j(t) + \sum_{i=-\infty}^{} \sum_{j=-\infty} d_{i;j} \psi_{i;j}(t) \tag{2.1}$$

In Eq. (2.1), the first summation gives a function that is a low resolution or coarse approximation of x(t), whereas the second summation gives a higher or finer resolution function. From Eq. (2.1), the expansion coefficient at a scale of i can be computed on the basis the expansion coefficient of a scale of $i + 1$ as

$$c_i(j) = \sum_{l} h(l - 2j) c_{i+1}(l) \tag{2.2}$$

$$d_i(j) = \sum_{l} g(l - 2j) c_{i+1}(l) \tag{2.3}$$

In which $h(t)$ and $g(t)$ denote the impulse responses of low-pass (LP) filter and high-pass (HP) filter that decompose the original signal into the approximation (e.g., low frequency) and detail components (e.g., high frequency). The signal is then down-sampled to divide into every two signals so that the signal's length does not change. At the next stage, the LP signal is also decomposed using complementary filters as LP filter and HP filter. The procedure of multi-resolution decomposition of a signal S_T is shown in Figure 2.4, where S_T, $h(t)$ and $g(t)$ denote the raw signal, LP filter and HP filter, respectively. Each stage consists of two digital filters and two down-samplers by 2. At a result, the two-band wavelet

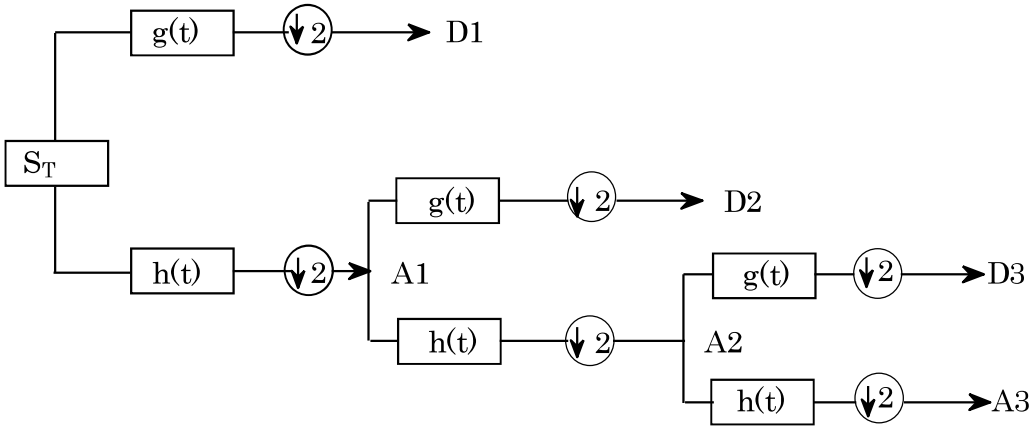

Figure 2.4 The three-scale WD tree, where h(t) is the LP filter and g(t) is the HP filter

system leads to a logarithmic frequency resolution. It is a fact that the low frequency components have narrow bandwidths and the high frequency components have wide bandwidths. This is called econstant-Qf filtering and is appropriate for some applications [46; 47; 48]. In wavelet-based pre-processing, suppose the original signal recorded using any stethoscope by S_T, where a bit-depth is 16 bits and sampling frequency is 44.1 kHz. Nextly, WD was used for cancellation of the unwanted frequency components over 700 Hz. The MATLAB program was used for the WD implementation. Daubechies Db10 type wavelet [43; 49], a good choice for our purpose as it deals with biomedical signals very well, was used as a mother wavelet. By applying the WD to signal S_T to 10 level, the frequency distribution for every level shown in Figure 2.5, the approximation coefficient (cA10)$(0-21.5$ Hz) was used to cut off the low frequency components below 21.5 Hz and the detail coefficient(cD5)$(689-1378$ Hz) was used for eliminating the high frequency components over 689 Hz. So the resulting signal X with band

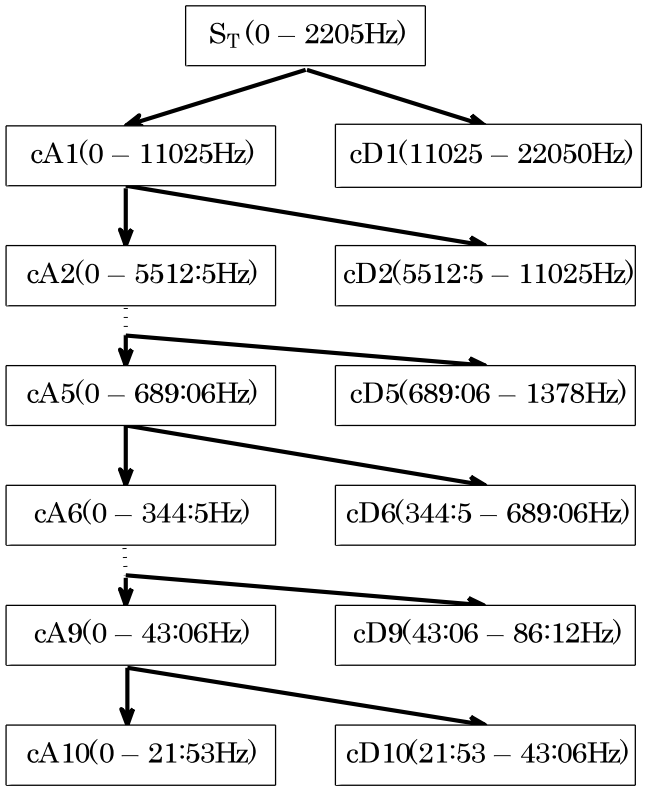

Figure 2.5 The frequency distribution of every level for by applying the WD to signal S_T to 10 levels

limit of 21.5 – 689 Hz was reconstructed by the components of cD10–cD6. At last, the normalization was applied by setting the maximum of the signal X to a value of 1.0.

2.3 Summary

In this section, firstly, the original heart sound signal noted by S_T is recorded from the tricuspid area using any stethoscope, where a bit depth is 16 bits and sampling frequency is 44.1kHz. And then based on the frequency range of heart

sound and Daubechies Db10 type wavelet is a good choice as mother wavelet for dealing with biomedical signals very well, By applying the WD to signal S_{T} to 10 level, the approximation coefficient (cA10)($0-21.5$ Hz) was used to cut off the low frequency components below 21.5 Hz and the detail coefficient(cD5)($689-1378$ Hz) was used for eliminating the high frequency components over 689 Hz. Finally, the resulting signal X with band limit of $21.5-689$ Hz was reconstructed by the components of cD10−cD6.

Chapter 3

Features extraction and heart sounds segmentation

3.1 Heart sounds Envelope (E_{T}) extraction in the time domain

The envelop cardiac sounds characteristic waveform (CSCW) proposed in our studies [50; 51] has been reported to provide sufficient performance compared to conventional Shannon envelope and Hilbert envelope algorithms which are used as the empirical or manual way and the automatic selecting way to estimate cardiac sound segmentation. However, the unexpected noises are still difficult problem in this methods. To overcome this points, the researcher [18] proposed a novel envelope (E_{T}) for heart sounds based on the Viola integral method. This study showed E_{T} is effective against not only amplitude variation, but also complex background and noise. This idea is described in following.

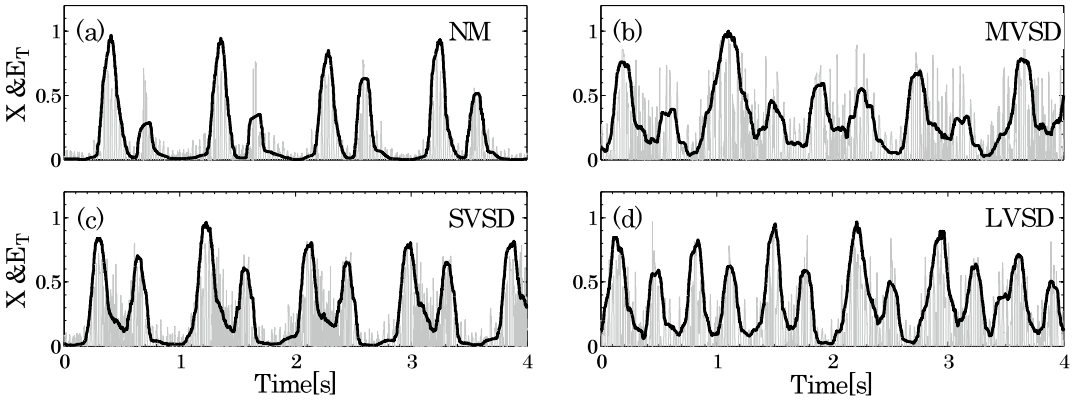

Figure 3.1 The analysis results for NM1 and NM2, the X(n) is daubed with gray, and the waveform E_T is plotted in black lines.

Consider a data series $X(n)$ preprocessed by wavelet decomposition for cardiac sounds signal $S_T(n), n = 1, 2, ..., N$, where N denotes the number of data. The envelop E_T is obtained by

$$E_T(m) = \frac{1}{2L_T + 1} \sum_{k=m-L_T}^{m+L_T} \left(X(k) - \overline{X}(k)\right)^2, m = L_T + 1, L_T + 2, \ldots, N - L_T, \tag{3.1}$$

where,

$$\overline{X}(k) = \frac{1}{2L_T + 1} \sum_{i=m-L_T}^{m+L_T} X(i). \tag{3.2}$$

L_T is the window width at point k. Since the studies [50; 52] have shown that the duration of S1 or S2 is about 0.05 s, in following study $L_T = 0.5 \times 0.05 \times F_S = 1225$ is set. Finally, the normalization is applied by setting the maximum amplitude of E_T to 1.

As an analysis results, the envelopes for typical NM, SVSD, MVSD and LVSD sounds are plotted in Figure 3.1. Figure 3.1(a) shows the X of NM sound and its E_T; Figure 3.1(b) shows the X of SVSD sound and its E_T ; Figure 3.1(c) plots

the $X(n)$ of MVSD sound and its E_{T}; Figure 3.1(d) plots the X of LVSD sound and its E_{T}. Here the X is daubed with gray, and the waveform E_{T} is plotted in black lines.

3.2 Heart sounds Envelope (E_{F}) extraction in the frequency domain

In the frequency domain, many researches [16; 19; 20; 21; 22; 23; 24; 25; 26; 27; 28; 29; 30] have been concerning on the characteristic extraction by local frequency analysis method. In the spectral analysis, short-time Fourier transform (STFT) [19; 20; 21; 22], the wavelet or wavelet packet decomposition [22; 23; 24] are commonly used. However, in our previous studies [31], envelope based two diagnostic features [Fmax, Fwidth] to detect heart murmurs has been verified as an efficient method because the highest classification accuracies were achieved for classifying normal and abnormal HSs. Fmax describes the maximum peak of the characteristic waveform and Fwidth is the frequency width between the crossed points of the characteristic waveform on a selected threshold value. However, it is a pity that there was not detail explain about how to select about one cardiac cycles. In order to extract the envelope for every cardiac cycle, first we segment heart sound into every cycle. And then extract heart sounds envelope E_{F} for every cardiac cycle.

3.2.1 Heart sounds segmentation

Basic heart sound signals are mostly comprised of four sound types: two outstanding sounds S1 and S2, and two weak sounds named as the third (S3) and the fourth heart sounds (S4). Although these four sounds may be audible by the auscultation of heart and occur in the frequency range of $20 - 2000$ Hz, since S3 and S4 appear at very low amplitudes with low frequency components and are difficult to be caught in usual auscultation, in the meanwhile, the unitary murmurs as a systolic ejection murmur (e.g., aortic stenosis) and a pan systolic murmur (e.g.,mitral regurgitation) mostly appear between the S1 and S2 with different noise patterns like the diamond and rectangular shapes [50]. Therefore, the S1 and S2 analysis play an important role in the heart sound analysis, in other words, to obtain the more information about S1 and S2, the segmentation of heart sounds might be an important pre-processing for the automatic analysis and classification of heart sounds.

In recent years, the studies of heart sound segmentation can be summarized into three categories as follow:

(1). With the reference ECG, the performance of the heart sound segmentation is quite good [53; 54]. However, the ECG, which is another signal source, may not be convenient for use in a medical check-up. Furthermore, in cases of infants or newborn children, placing the leads on a newborn is difficult because of limited space on the torso and the babies are not cooperative. Furthermore, performing an ECG on a newborn using the current complicated leads system by inexperienced nurses is prone to error, such as wrong leads placement, artifacts, and inadequate ECG signal acquisition.

(2). The the frequency domain based segmentation algorithm was proposed by tracking of heart sound spectrum [37; 55; 56; 57]. With the aid of frequency domain analysis, certain frequency components are first extracted according to the the time domain characteristics; and the start and end points of each cycle are determined by using the time domain search method at a given threshold value. However, the selection of threshold and filtering of the unexpected noise are still difficult problems in this kind of methods and few literature mentions this issue

(3). The envelope based segmentation method were studied by many researches [50; 51], our previous study [58] reported that cardiac sound characteristic waveform (CSCW) method provided sufficient performance compared to conventional Shannon envelope and Hilbert envelope algorithms which were used as the empirical or manual way and the automatic selecting way to estimate cardiac sound segmentation. However, the selection of threshold and filtering of the unexpected noise are still difficult problem in this kind of methods. To overcome this points, the researcher [18] proposed a novel method for the segmentation of heart sounds. In this paper, characteristic waveform (CW) of heart sounds and the center moment character (CMW) of CW based on the Viola integral method were proposed first. And then each heart sound cycle can be quickly found by CMWs local extreme points. This paper showed CW is effective against not only amplitude variation but also complex background and noise. Moreover, using CMWs local extreme points method for locating the segmentation not only avoids the difficulty of setting multiple thresholds to detect S1 or S2, but also overcome the

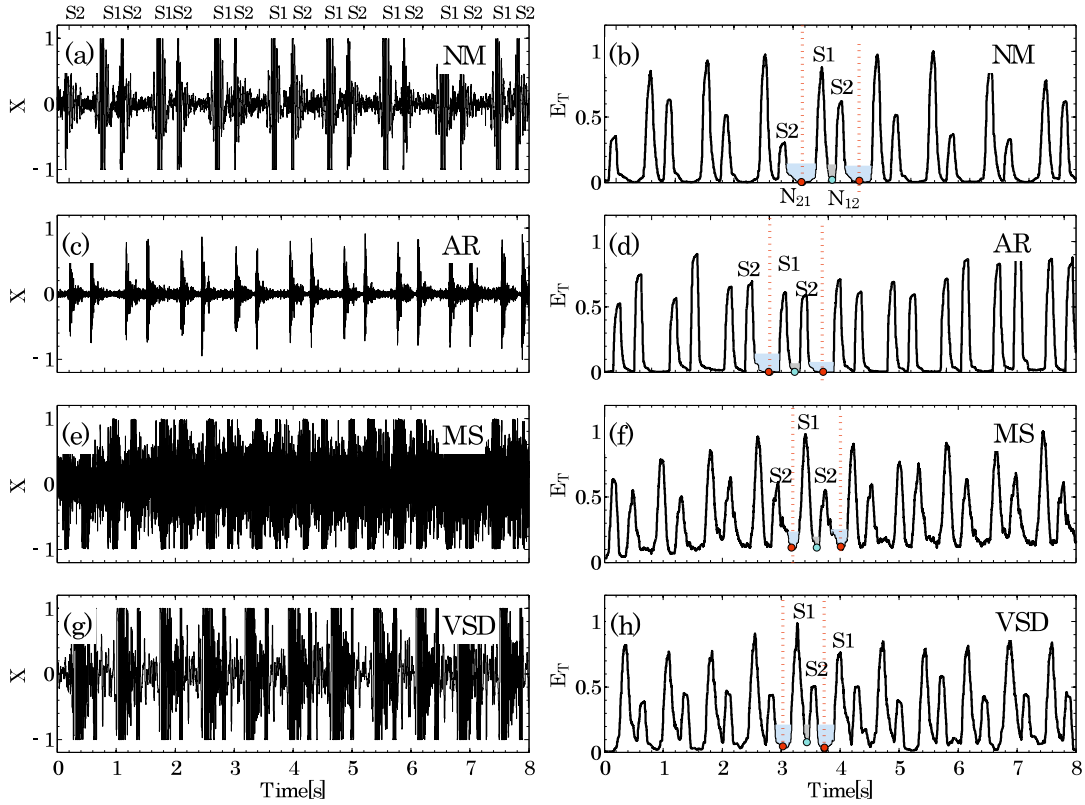

Figure 3.2 Examples of a very typical normal sound and 3 typical abnormal sounds. The left parts of this figure show the filtered heart sound signal X and the right part show the E_T corresponding to the left part.

detections of the start and end points of the sounds (S1 or S2) drowned in the murmurs. However, this paper does not provide the detailed method to locate the CMWs local extreme points. Furthermore, the CMW might have the different amplitude or the same amplitude for every cycle because of the complexity of CW. Therefore, it is very difficult to search the local extreme points of the CMW, let alone locate the local extreme points automatically.

In this section, a Moving Windowed Hilbert Transform (MWHT) method was proposed for automatic locating the local maxima and minima task by using the properties of the Hilbert-transform. The Hilbert transform plays an important

role in the theory and practice of signal processing, and it has been widely used in many areas, such as edge detection [59; 60], peak detection [61], and so on. The study [61] considered the even function, $f(t) = 1/(1+t^2)$ as a R-wave envelope model. The Hilbert transform of $f(t)$, is given by $\hat{f}(t) = t/(1+t^2)$. Therefore, the maximum value of the envelope function $r(t)$ corresponds to the zero crossing point of the $\hat{r}(t)$ which is referred as odd-symmetry function. Since the heart sounds too complicated to consider the its envelop as an even function like $f(t) = 1/(1+t^2)$. However, according to the envelope of heart sounds such as the envelopes plotted in Figure 3.2. Figure 3.2 plots the normalized X of four typical heart sound signals and its envelope curve E_{T} extracted by the Viola integral approach. Figure 3.2(a) shows the case of the typical normal sound and its E_{T} is showed in Figure 3.2(b). An abnormal case of the typical aortic regurgitation and its E_{T} are shown Figure 3.2(c) and (d). Figure 3.2(e) and (f) show an abnormal case of the typical mitral stenosis. an abnormal case of the typical ventricular septal defect and its E_{T} are shown in Figure 3.2(g) and (h). Figure 3.2(e) and (f) also show that this method is effective against not only amplitude variation but also complex background and noise. Furthermore, notice that the E_{T}, not only for normal case plotted in Figure 3.2(b) but also for abnormal cases plotted in Figure 3.2(d), (f) and (h), the most important characters of E_{T} are summarized as follow.

(1). The area (marked by gray) close to the nadir from S1 to S2 (named as N_{12}, and marked by •) is basically considered as an even convex function symmetrical with respect to the vertical line (marked by blue) crossing the N_{S12}.

(2). The area (marked by gray) close to the nadir from S2 to S1 (named as N_{21}, and marked by •) is also basically considered as an even concave function symmetry with respect to the vertical line(marked by red) crossing the N_{21}.

N_{12} can be considered as the segmentation point from S1 to S2. N_{21} can be considered as the segmentation point from S2 to S1. Therefore, locating the points N_{12} can separate the S1 and S2, and locating the points N_{21} can segment every cardiac cycle. For these reasons, the automatic locating points method proposed is detailed as follow subsection.

3.2.1.1 Continuous-Time Moving Windowed Hilbert Transform

The moving windowed Hilbert transform $MWHT(f(t))$ of a function $f(t)$ is defined by

$$MWHT_{\mathrm{f}}(t) = \check{f}(t) = \frac{1}{\pi} \int_{-\infty}^{1} \frac{W(\tau - t) f(\tau)}{t - \tau} d\tau \tag{3.3}$$

where W is a window with the length W_τ. Figure 3.3 shows the principle of $MWHT(f(t))$. In fact, the value of $\check{f}(t)$ is the center value of the Hilbert transform of $W(\tau - t) f(\tau)$ at the interval τ 2 $[t - \frac{\mathrm{W}_\tau}{2}, t + \frac{\mathrm{W}_\tau}{2}]$. The Moving windowed Hilbert transform of the derivative of a function is equivalent to the derivative of the Moving windowed Hilbert transform, that is

$$\frac{d}{dt}\check{f}(t) = \frac{1}{\pi} \int_{-\infty}^{1} \frac{(W(\tau - t) f(\tau))^{0}}{t - \tau} d\tau. \tag{3.4}$$

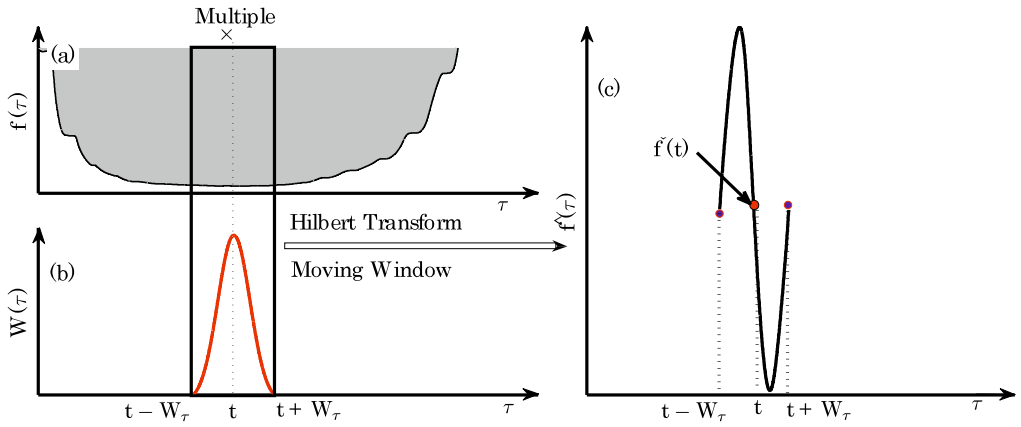

Figure 3.3 The schematic diagram of MWHT

Suppose $W(\tau - \mathrm{T1})\mathrm{f}(\tau)$ is a concave even function with a nadir and symmetrical with T1 like $f_1(t)$ plotted in Figure 3.4, then the derivative of the function $W(\tau - \mathrm{T1})\mathrm{f}(\tau)$, $(W(\tau - \mathrm{T1})\mathrm{f}(\tau))^0 < 0(\tau \geq \mathrm{T1})$. If we substitute $\mathrm{T1} - \tau$ with τ_1, then $W(\tau_1)f(\tau_1 - \mathrm{T1})$ is also concave even function, and $(W(\tau_1)f(\tau_1 - \mathrm{T1}))^0$ is an odd function and $(W(\tau_1)f(\tau_1 - \mathrm{T1}))^0 < 0(\tau_1 \geq \mathrm{T1})$. Based on Eq. (3.3) the $\check{f}(\mathrm{T1})$ is computed as

$$\check{f}_1(\mathrm{T1}) = \mathrm{WMHT}[\mathrm{f}_1(\mathrm{T1})] = \frac{1}{\pi}\int_{-\infty}^{1} \frac{\mathrm{W}(\tau - \mathrm{T1})\mathrm{f}_1(\tau)}{\mathrm{T1} - \tau}\,\mathrm{d}\tau. \tag{3.5}$$

If we substitute $\mathrm{T1} - \tau$ with τ_1 and then we get

$$\check{f}_1(\mathrm{T1}) = \frac{1}{\pi}\int_{-\infty}^{1} \frac{\mathrm{W}(\tau 1)\mathrm{f}_1(\tau_1 - \mathrm{T1})}{\tau_1}\,d\tau_1 = 0. \tag{3.6}$$

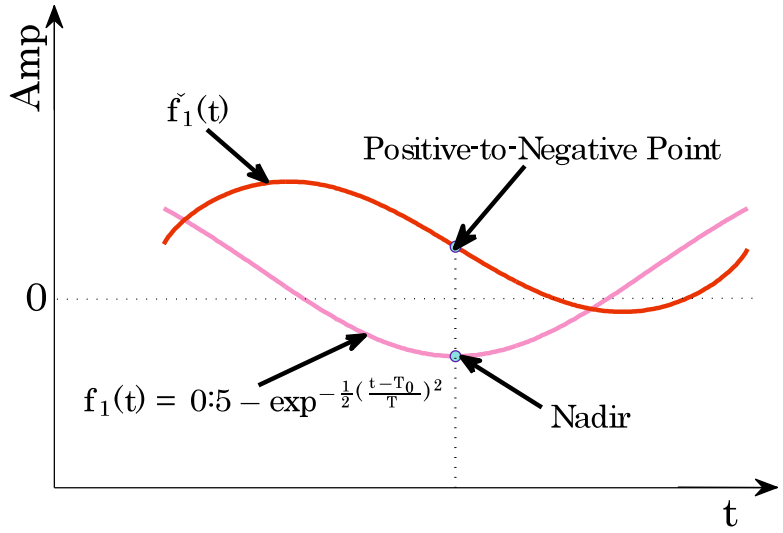

Figure 3.4 Illustration of the minimum finding principe. The minimum value of the concave even function $f_1(t)$ corresponds to the negative-to-positive point of the $\check{f}_1(t)$.

Based on Eq. (3.4) the $\check{f}_1^{\,0}(T1)$ is computed as

$$\check{f}_1^{\,0}(T1) = MWHT[f_1^{\,0}(T1)] = \frac{1}{\pi}\int_{-\infty}^{1} \frac{(W(\tau - T1)f(\tau))^0}{T1-\tau}\,d\tau. \tag{3.7}$$

If we substitute $T1-\tau$ with τ_1 and then we get

$$\check{f}_1^{\,0}(T1) = \frac{1}{\pi}\int_{-\infty}^{1} \frac{(W(\tau_1)f_1(\tau_1 - T1))^0}{\tau_1}\,d\tau_1 = \frac{2}{\pi}\int_{T1}^{1} \frac{(W(\tau_1)f_1(\tau_1 - T1))^0}{\tau_1}\,d\tau_1 < 0. \tag{3.8}$$

That is the nadir of the convex function corresponds to the positive-to-negative transition points of its moving windowed Hilbert transform function. Here, the

gaussian function $f_1(t)$ as a concave even function is taken as an example to analyze. The graphical representation of the $f_1(t)$, $\check{f}_1(t)$, are shown in Figure 3.4. Based on these properties of Hilbert transform combined with the points mentioned about the envelope of heart sounds, a moving windowed Hilbert transform method proposed to search the peaks and nadirs of the envelope is detailed as the next section.

3.2.1.2 Segmentation points locating logic

According to the important characters of E_{T} summarized in Pages 22 – 23, every period (named as $X_{\mathrm{P_i}}$) of heart sound can be located. According to properties of Hilbert transform about a concave even function and a convex even function summarized in the section 3.2.1.1, Based on the t-axis of the positive-to-negative points (PNP) of the $\check{E}_{\mathrm{T}}$ correspond to the t-axis of the nadirs in the E_{T}, the heart sounds can be segmented into every cardiac cycle. The detailed segmentation procedure showed in Figure 3.5 is summarized as follows:

(a). Firstly, in the time domain, the envelope E_{T} like the black lines plotted in Figure 3.5(a) for normal sound and Figure 3.5(b) for VSD sound are extracted from the heart sounds X like yellow lines plotted in Figure 3.5(a) and (b).

(b). Secondly, based on Eq. (3.3), The $\check{E}_{\mathrm{T}}$s like black lines plotted in Figure 3.5(c) for normal sound and Figure 3.5(d) for VSD sound are generated for E_{T}s plotted in Figure 3.5(a) and (b).

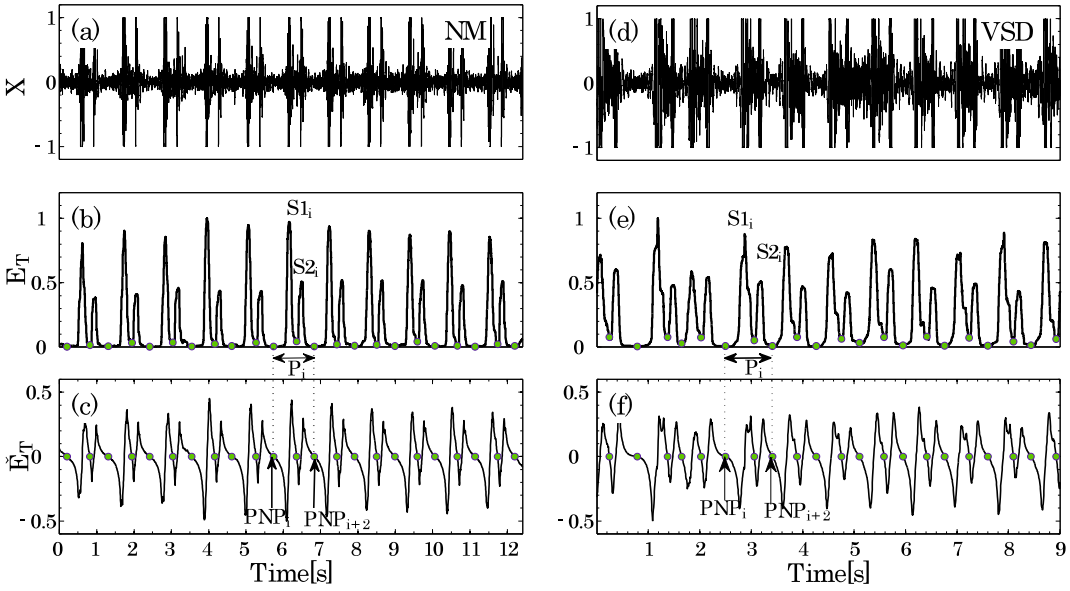

Figure 3.5 Example for segmentation logic for NM case and VSD cases. The $\check{E}_T$ plotted in (c) and (f) are generated by Gaussian Window with the W_N = 1s.

(c). Finally, the PNP (marked by •) in Figure 3.5(c) and (d) are determined by

$$\text{PNP} = i, \quad \text{if} \quad \begin{cases} \check{E}_T(i) = 0 \\ \check{E}_T(i-1) \geq 0 \\ \check{E}_T(i+1) \leq 0 \end{cases}. \tag{3.9}$$

Then X_{P_i} representing i-index cardiac cycle (Figure 3.5(a) and (b)) is calculated by

$$X_{P_i} = X(\text{PNP}_{i+2}) - X(\text{PNP}_i). \tag{3.10}$$

Therefore, the heart sound X is divided into $X_{P_i}(i = 1, 2, \ldots, I)$, where I is the number of cardiac cycles included in heart sound X. Therefore, by identifying

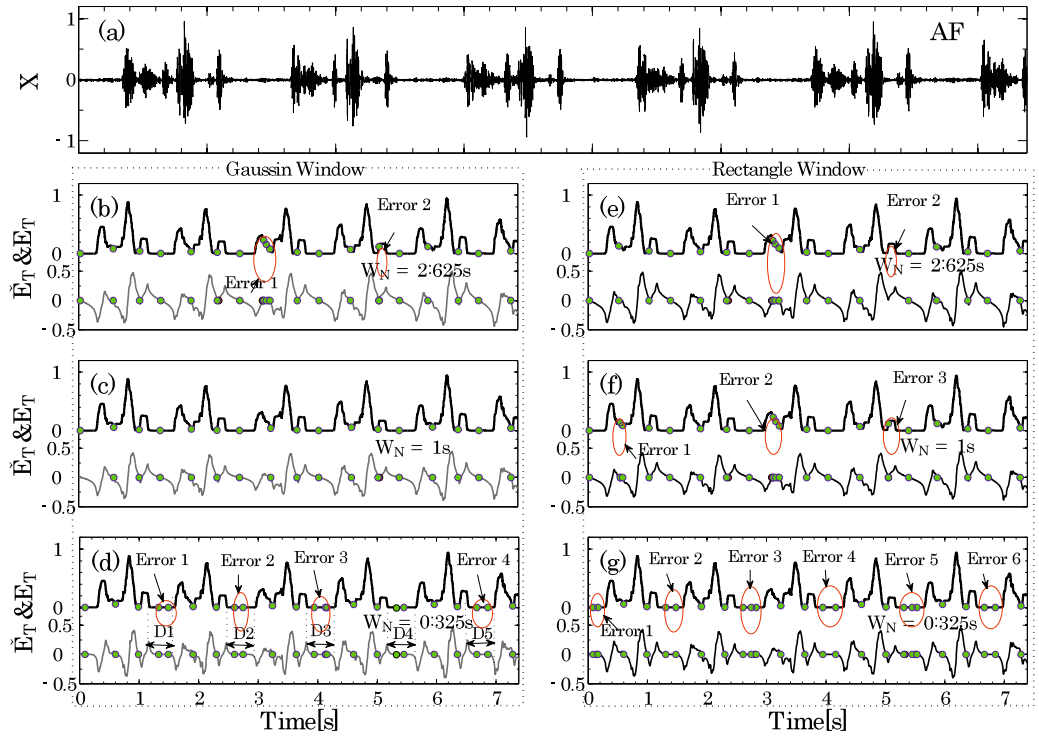

Figure 3.6 Example for comparative analysis the located points for AF case using different window and different window width. The $\check{E}_T$ plotted in (b), (c) and (d) are generated by Gaussian Window with the W_N = 2:625s; 1s; 0:325s, respectively. The $\check{E}_T$ generated by Rectangle Window with W_N = 2:625s; 1s; 0:325s are plotted in (d), (e) and (f), respectively

the PNP of the $\check{E}_T$, the cardiac cycle segmentation can be located. However, whether the located points are the real points of the E_T or not will be affected from the selected window and its width. In other words, for different window and different length, the located points may not be the real points of $\check{E}_T$ of the filtered signal X. Therefore, it is necessary to choose the appropriate window and its width. In order to illuminate these problems more clearly, the examples for different window and different length are analyzed and the analysis results are showed in Figure 3.6.

Figure 3.6 shows that the AF case whose nadir points from S2 to S1 are very different to be located. Figure 3.6(a) shows the filtered signal X. Figure 3.6(b)-(d) show that the $\check{E}_{\mathrm{T}}$ and the located points for $\hat{E}_{\mathrm{T}}$ using the Gaussian Window usually used in signal processing. Figure 3.6(e)-(g) show the $\check{E}_{\mathrm{T}}$ and the located points for $\hat{E}_{\mathrm{T}}$ using the Rectangle Window which is an ordinary window. From the results plotted in Figure 3.6, we can see that

(1). Because the $W_{\mathrm{N}} = 0.325s$ is smaller than the width which is about 0.5s such as D1, D2, D3, and D4 in Figure 3.6(d), the false points are generated such as Error 1-4 in Figure 3.6(d) and Error 1-6 in Figure 3.6(g).

(2). Since the $W_{\mathrm{N}} = 2.625s$ is very big, on some place the false points might be generated such as the Error 1 in Figure 3.6(b) and Error 2 in Figure 3.6(e), and on some place the true points might be lost such as Error 2 in Figure 3.6(b) and Error 2 in Figure 3.6(c).

(3). Since the windowed X using Gaussian window is more smoother than that using Rectangle Window, there are no errors in Figure 3.6(c), but there are 3 errors including false points Error 1 and Error 2 and lost point Error 3 in Figure 3.6(f).

Therefore, in order to avoid generating the false points such as the Errors in Figure 3.6(d) and (g), the window width W_{N} must be greater than the width of two consecutive convex such as D1, D2, D3, and D4 in Figure 3.6(d). In order to avoid generating the false points such as Error 2 and losing the real points such as Error 3 in Figure 3.6(f) at the same window wide, the window is selected the smooth Gaussian Window in this paper. In order to avoid losing the real point

such as Error 2 in Figure 3.6(b) and Error 2 in Figure 3.6(e) and generate false points such as Error 1 in Figure 3.6(b) and Error 2 in Figure 3.6(e), the window width W_{N} is not supposed to be too long but supposed to be greater than one cycle of heart sounds, especially for not regular heart sounds such AF case in Figure 3.6(a). Since the heart beats are from 60 to 120 per minute [62; 63], the maximum of heart sound cycle is about 1 s. In order to make the part from S2 to S1 included in the window, comparing the experimental analysis, in this paper the W_{N} is set as 1 s.

3.2.1.3 Performance evaluation

The proposed segmentation points detection method was evaluated using the two parts of heart sounds recorders. One part was detected from Chinese hospital during the period from 2011 to 2012 and its sampling frequency is 44.1kHz. It contained 3390s CHD sounds which consisted of 620s ASD from 14 patients, 270s F4 from 7 patients, 550s PDA from 10 patients, 1290s VSD from 33 patients ASD and 660s mixed CHD from 12 patients and 3940s RHD sounds. The other part was download from Michigan heart sounds database [64]. Its contained total 1496.8s length 23 cases (named as M01, M02,...,M23) recordings sampled at 44.1kHz.

To evaluate the performance of this segmentation method, we calculated the quantitative results: missing nadir 12 (MN12) when a nadir from S1 to S2 is missed, false nadir 12 (FN12) when a false nadir from S1 to S2 is generated, true cardiac cycle (TCC) when the cardiac cycle is correctly detected, and false cardiac cycle (FCC) when the cardiac cycle is not correctly detected. Therefore, the accuracies for cardiac cycle (ACC) can be computed by using the following

equations, respectively

$$\mathrm{ACC} = \frac{\mathrm{TCC}}{\mathrm{TCC} + \mathrm{FCC}} \times 100\% \tag{3.11}$$

[18] has introduced a segmentation method which was better than DWT method. A complete segmentation [18] is described briefly as follows.

(a). The E_{T} by setting the parameter 0.05 s and the CMW by setting the parameter 0.5s was extracted.

(b). The maximum points sequence extracted from CMW was viewed as the close boundaries of each cycle. The minimum points sequence extracted from CMW was viewed as the center of every cycle.

Figure 3.7 plotted two examples for two clinical heart diseases using our method and [18]'s method. Figure 3.7 showed that it is difficult to locate the segmentation points using the maximum and the minimum of the CMW for these cases. If we select the threshold value to select maximum and minimum points on CMW, then it is also difficult to select threshold value. However, using our method it is very easy. Furthermore, since our method locate the points by the pass-zero points, it do not need the threshold value. Table 3.1 shows that the analysis results of analyzing the data in this section using our method and [18]'s method. Based on the results of Table 3.1, the proposed method achieved significantly better performance than [18]'s methods. we concluded that the proposed method can not only improve the accuracy of cardiac cycles but also automatically locate using the pass-zero points. Furthermore, the proposed method does not require

Table 3.1
Performance evaluation of the proposed method and [18]'s method using the clinical data and Michigan heart sounds data

Rec	ACC(%)	
	[18]'s method	Our method
PDA	89	98
RHD	81	96
NM	100	100
ASD	89	99
VSD	78	95
F4	91	99
M01	100	100
M02	100	100
M03	100	100
M04	100	100
M05	100	100
M06	100	100
M07	100	100
M08	100	100
M09	100	100
M10	100	100
M11	100	100
M12	100	100
M13	100	100
M14	100	100
M15	100	100
M16	100	100
M17	100	100
M18	100	100
M19	100	100
M20	100	100
M21	100	100
M22	100	100
M23	100	100

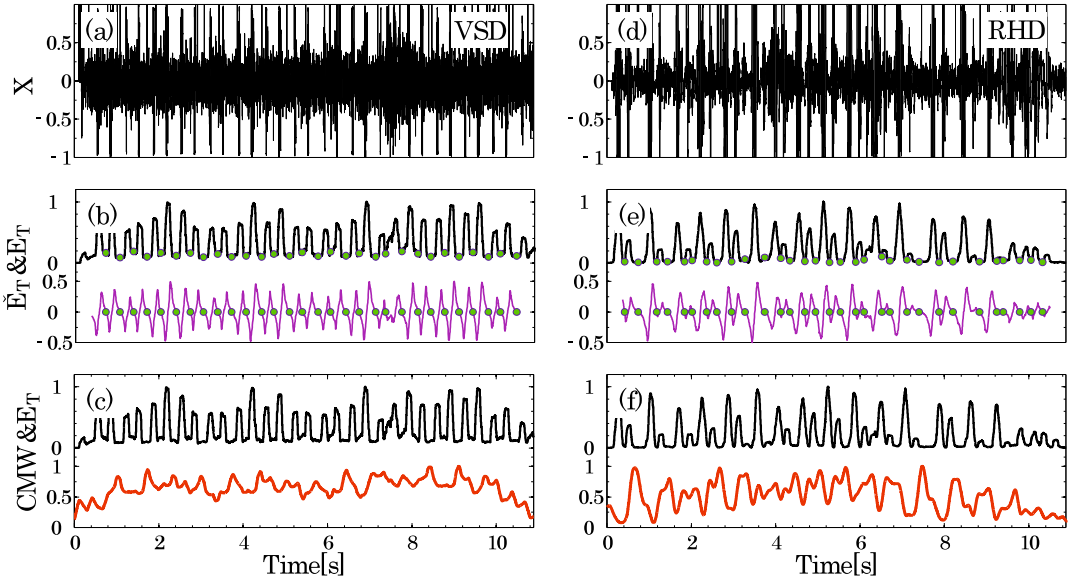

Figure 3.7 The examples for two clinical heart diseases. (a) plots the VSD cases and (d) plots the RHD cases. (b) and (e) correspond to the VSD case in (a) and the RHD case in (d) by using our method. (c) and (f) plots the CW and CMW using the Yan2010 method. Here CW is E_T, CMW is gained with 0.5s parameter.

additional decision rules with sets of thresholds based on the amplitude of S1 or S2.

3.2.2 Heart sounds segmentation based the envelope E_F extraction

For every cardiac cycle, in the frequency domain, the envelope (E_F) in the frequency domain is obtained by the moving average method as follows: For i-index cardiac cycle X_{P_i} , the envelope E_{F_i} is obtained by

$$E_{F_i}(k) = \frac{1}{2L_F + 1} \sum_{l=k-L_F}^{k+L_F} |X_{F_i}(l)|, k = L_F, ..., N_i - L_F, \tag{3.12}$$

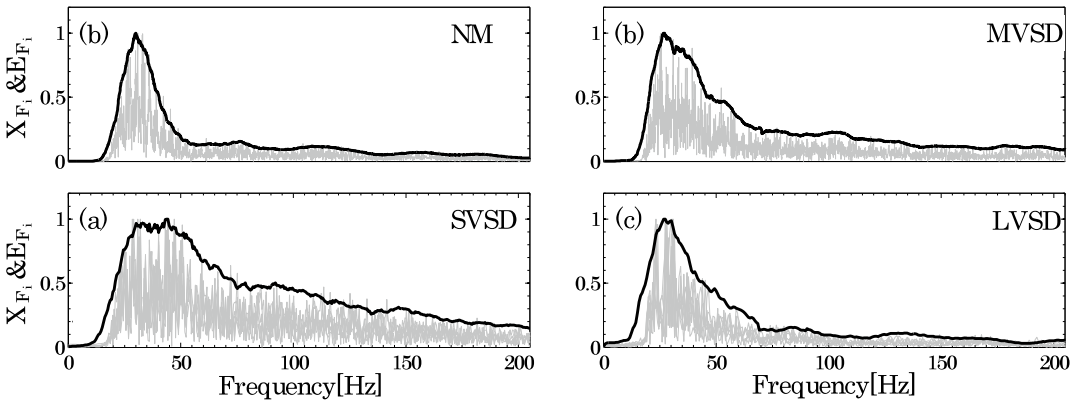

Figure 3.8 The analysis results for NM, SVSD, MVSD, and LVSD examples, the X_{F_i}s is daubed with gray, and the waveform E_{F_i}s are plotted in black lines.

where

$$X_{F_i}(l) = \sum_{n=1}^{N_i-1} X_{P_i}(n) \exp\left(-j\frac{2\pi}{N_i}nl\right), \quad l = 0, 1, 2, \ldots, N_i - 1 \tag{3.13}$$

N_i is the length of X_{P_i}, and $2L_F$ is the window width. Since the width of frequency is generally greater than 16 Hz, then $L_F = 8\times(F_s)/(N_i)$ is set in following analysis. moreover, E_{F_i} is also normalized. As an analysis results, the envelopes for i-index cardiac cycle of NM, SVSD, MVSD and LVSD sounds are plotted in Figure 3.8. Figure 3.8(a) shows the X_F of NM sound and its E_F; Figure 3.8(b) shows the X_F of SVSD sound and its E_F; Figure 3.8(c) shows the X_F of MVSD sound and its E_F ; Figure 3.8(d) plots the X_F of LVSD sound and its E_F. Here the X_F is daubed with gray, and the waveform E_F is plotted in black lines.

3.3 Diagnostic features definition

As mentioned in the study [50], the time interval between two abutted S1,the interval between S1 and S2, the width of S1, and the width of S2 are very important parameters for detecting heart disorders. A simple way to calculate these intervals is to measure the peaks of S1 and S2. However the extracted peaks sometimes are not correct especially for strong murmurs heart sound. To solve this problem, in this study, the centers of segments of S1 and S2 are considered. The concept for defining the diagnostic parameters in the time domain is described in Figure 3.9(a). H_{T} is the threshold and should be selected at a suitable value. The left and right points on the curve E_{T} crossed by H_{T} line are defined as $L_{\mathrm{k}}(i)$ and $R_{\mathrm{k}}(i)(\mathrm{k} = 1, 2; \mathrm{i} = 1, 2, \ldots, \mathrm{M})$ in a sequential order. The gravity centers of $\mathrm{S1_i}$ and $\mathrm{S2_i}$ segments are defined by $G_1(i)$ and $G_2(i)$, and obtained as follows:

$$G_{\mathrm{k}}(i) = \frac{\sum_{\mathrm{m}=L_{\mathrm{k}}(\mathrm{i})}^{R_{\mathrm{k}}(\mathrm{i})} m \times E_{\mathrm{T}}^2(m)}{\sum_{\mathrm{m}=L_{\mathrm{k}}(\mathrm{i})}^{R_{\mathrm{k}}(\mathrm{i})} E_{\mathrm{T}}^2(m)}, k = 1, 2 \tag{3.14}$$

So the time domain features $[T_{12}, T_{11}]$ are given by

$$T_{11}(i) = G_1(i+1) - G_1(i) \tag{3.15}$$

$$T_{12}(i) = G_2(i) - G_1(i). \tag{3.16}$$

In the frequency domain, the diagnostic features $[F_{\max}, F_{\mathrm{W}}]$ has been verified to be useful for detecting heart murmurs [31], where $F_{\max}$ is the frequency at the

maximun value and F_{W} is the corresponding width of character waveform over the given threshold value. However, the value $F_{\max}$, especially in VSD sounds, will be influenced much due to the heart murmurs. Instead of $F_{\max}$, the center of gravity $F_{\mathrm{G}}(i)$ for i-index cardiac cycle is considered as a frequency index, which is described in Figure 3.9(b), and is obtained as follows:

$$F_{\mathrm{G}}(i) = \frac{\sum_{k=1}^{[N_i=2]} k \times E_{\mathrm{F_i}}^2(k)}{\sum_{k=1}^{[N_i=2]} E_{\mathrm{F_i}}^2(k)} \tag{3.17}$$

The concept for defining the diagnostic parameters F_{W} is described in Figure 3.9(b). H_{F} is the threshold and should be selected at a suitable value. The left and right points on i-index envelope $E_{\mathrm{F_i}}$ crossed by H_{F} line are defined as $L_{\mathrm{F}}(i)$ and $R_{\mathrm{F}}(i)(i = 1, 2, \ldots, \mathrm{I})$ in a sequential order. The frequency width $F_{\mathrm{W}}(i)$ of i-index $E_{\mathrm{F_i}}$ is defined by $L_{\mathrm{F}}(i)$ and $R_{\mathrm{F}}(i)$, and computed by

$$F_{\mathrm{W}}(i) = R_{\mathrm{F}}(i) - L_{\mathrm{F}}(i). \tag{3.18}$$

To extract features in the time domain and the frequency domain, the value of H_{T} will be a suitable value between the interval [0.2, 0.4] and H_{F} has good performance in the interval [0.1, 0.2]. By experimental analysis, in this paper, the H_{F} is set at 0.2. Figure 3.9(c) and (d) show the plots of $[T_{12}, T_{11}]$ and $[F_{\mathrm{G}}, F_{\mathrm{W}}]$, which are extracted from samples of NM, SVSD, MVSD and LVSD respectively. From Figure 3.9, we find that

(1). In the time domain, SVSD is difficult to be discriminated from MVSD and NM, but in the frequency domain SVSD is very easy to be discriminated from MVSD and NM.

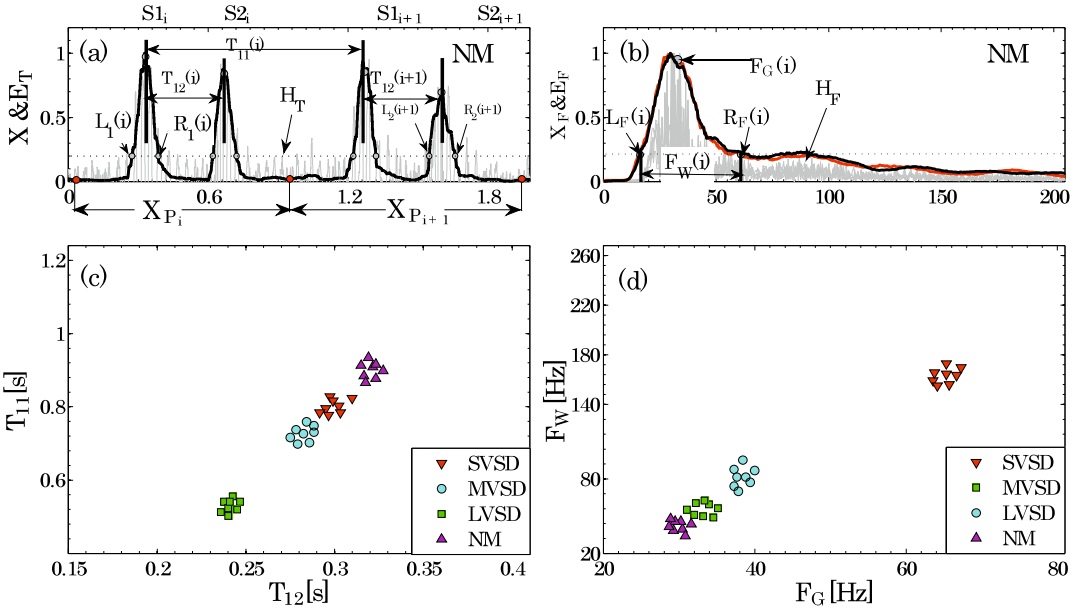

Figure 3.9 Definition of the diagnostic features $[T_{12}; T_{11}]$ & $[F_G; F_W]$ and their scatter diagram. (a) and (b) normal sound case, (c) and (d) VSD case, (g) scatter diagram of $[T_{12}; T_{11}]$, (h) scatter diagram of $[F_G; F_W]$.

(2). In the frequency domain, LVSD is difficult to be discriminated from MVSD and NM, but in the time domain it is easy to distinguish LVSD from MVSD and NM.

(3). In the frequency domain the distribution of MVSD is close to NM and LVSD, but in the time domain, MVSD is very different from NM and LVSD.

Therefore, the combination of feature parameters $[T_{12}, T_{11}]$ and $[F_G, F_W]$ will be powerful to discriminate VSD.

In order to build the heart sound features data sets (DSs), 242 normal heart sound samples (46 people in university, aged 23~27 years with a mean of 23.8) and 226 sound samples including 62 SVSD type sounds, 90 MVSD type sounds and 74 type LVSD sounds (37 patients in hospital, aged 4 ~ 14 years with a

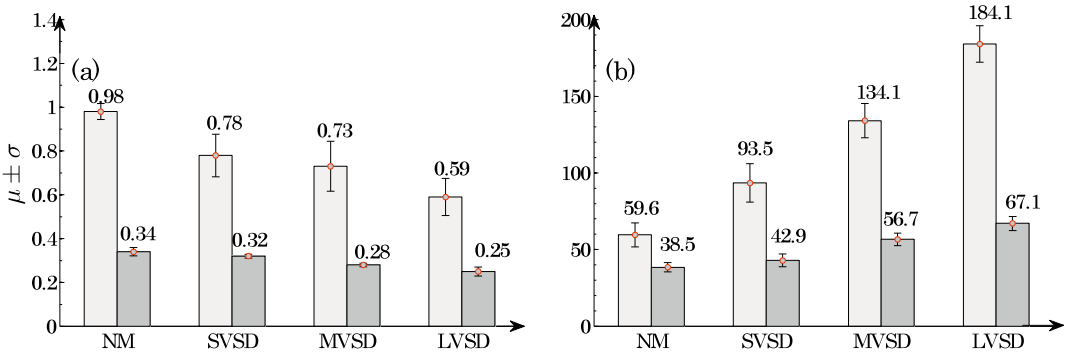

Figure 3.10 Summary of the statistical character of the data sets for NM cases and VSD cases. (a) $\mu \pm \sigma$ for $[T_{12}; T_{11}]$ in the time domain and (b) $\mu \pm \sigma$ for $[F_G; F_W]$ in the frequency domain

mean of 6.7) are analyzed. The mean values and standard deviations of T_{11} and T_{12} in case of NM1, NM2, SVSD, MVSD, and LVSD sounds are summarized and shown in Figure 3.10(a). The mean values and standard deviations of F_G and F_W in case of NM, SVSD, MVSD, and LVSD sounds are summarized and shown in Figure 3.10(b).

3.4 Summary

This section was very important because the diagnostic results were rooted in the diagnostic features. The definition of diagnostic feature were summarized as follow: Firstly, the E_T was obtained with emphasis on the first heart sound (S1) and the second heart sound (S2) by applying the Viola integral waveform method, and the parameter L_T was set as 0.6s. Secondly, to extract the E_F for every cardiac cycle, according to the character of E_T at the area from S2 to S1, a novel method named moving windowed Hilbert transform (MWHT) was proposed to segment the heart sounds into every cycle automatically. Moreover, how to

propose MWHT method, and how to set the window width and how to select the window for MWHT were described in detail. Finally, in the time domain the diagnostic features $[T_{12}, T_{11}]$, the width of two abutted S1 and the width between S1 and S2 at a threshold value, were extracted from the envelope E_{T}. In the frequency domain, the diagnostic features $[F_{\mathrm{G}}, F_{\mathrm{W}}]$, the frequency width and the gravity, were extracted from the envelope E_{F} for every cardiac cycle. AS the statistical analysis of $[T_{12}, T_{11}]$ and $[F_{\mathrm{G}}, F_{\mathrm{W}}]$, the 242 normal heart sounds and 226 VSD sound samples (62 SVSD sounds, 90 MVSD sounds and 74 LVSD sounds) were summarized. The analysis results showed that using $[T_{12}, T_{11}]$ and $[F_{\mathrm{G}}, F_{\mathrm{W}}]$ as diagnostic features would discriminate among VSD and NM sounds.

Chapter 4

Classification boundary function based on SVM

In this section, a classification boundary for feature DSs based on SVM technique is proposed to be used as the classifier to discriminate VSD from normal sounds. To generate a suitable classification boundary for the given feature DSs, according to the characters of SVM and ordinary classification accuracy achieved in many researches, another DSs generated artificially and CA-based the optimal feature searched automatically are described as follows.

4.1 A review on SVM

SVM have been proposed as an effective statistical learning method for classification of different data classes by the classification curves which are so called support vectors (SV) [65]. SVM have been used successfully for the solution of many problems including heart murmurs classification [31], cancer diagnosis [34],

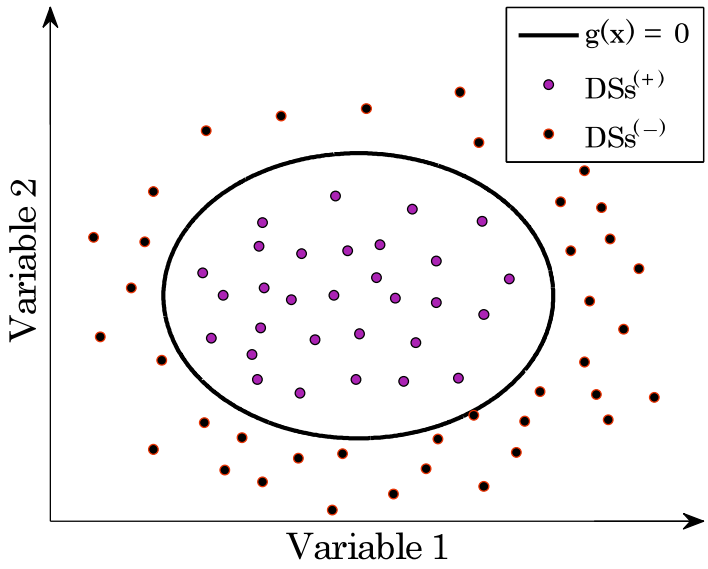

Figure 4.1 The example for nonseparable data sets which are denoted DSs^{-} and DSs^{+}, respectively. The classification boundary curve g = 0 which can classify the input data

handwritten digital recognition [35], etc.

The main purpose of SVM is to find a classification boundary curve $g(x) = 0$(see Figure 4.1), which has deviated away from all the training DSs and is used to obtain the classification function $f(x)$. When the separating samples belong to linear inseparable classes, generally, a non-linear mapping, usually defined as $\phi(\cdot) : R^{n} \; ! \quad R^{nh}$, is used to map the input vector into a high dimensional feature space. In this case, the classification function $f(x)$ is defined by

$$f(x) = sign(g(x)), \tag{4.1}$$

$$\text{where} \quad g(x) = W^{T}\phi(x) + b. \tag{4.2}$$

Where x is an input vector, W is an adjustable weight vector, b is a bias, and $g(x)$ is the discriminant function. Consider the two classes training DSs consisting of

the positive DSs $DSs^{(+)}$ and negative DSs $DSs^{(-)}$. According to the structural risk minimization inductive principle and the Kuhn Tucker optimization theory [66], the approach to solve $g(x)$ can be written as a classic quadratic optimization problem

$$\max_{\alpha} Q(\alpha) = \sum_{i=1}^{N} \alpha_i - \frac{1}{2} \sum_{i=1}^{N} \sum_{j=1}^{N} \alpha_i \alpha_j y_i y_j \phi^T(DSs_i)\phi(DSs_j) \quad (4.3)$$

$$\text{subject to} \quad \sum_{i}^{N} \alpha_i y_i = 0, \quad 0 < \alpha \leq C, \quad (4.4)$$

where DSs_i is the ith DSs instance, $y_i \in \{+1, -1\}$ is a label that determines the class of DSs_i, and C is a user-defined positive finite constant. A larger C means a higher penalty and usually is assigned to empirical errors. The solution of Eq. (4.3) should satisfy

$$\alpha_i \left[y_i \left(\sum_{j=1}^{N} \phi^T(DSs_j)\phi(DSs_i) + b \right) - 1 \right] = 0, \quad i = 1, 2, \ldots, N, \quad (4.5)$$

which has non-zero multipliers if and only if the points (termed SV) satisfy

$$y_i \left(\sum_{j=1}^{N} \alpha_j y_j \phi^T(DSs_j)\phi(DSs_i) + b \right) - 1 = 0 \quad (4.6)$$

The $g(x)$ is determined by the SV which is a small subset of the training vectors. Here, $\phi^T(DSs_i) \cdot \phi(DSs_j)$ can be replaced by a kernel function

$$k(DSs_i, DSs_j) = \phi^T(DSs_i) \cdot \phi(DSs_j) \quad (4.7)$$

$k(DSs_i, DSs_j)$ may be any of the symmetric functions that satisfy the Mercel conditions [67] and perform the non-linear mapping into feature space. In this

paper, the Gaussian function is selected as the kernel function.

$$k(\mathrm{DSs_i}, \mathrm{DSs_j}) = \exp\left(-\frac{\mathrm{kDSs_i - DSs_j k^2}}{2\tau^2}\right) \tag{4.8}$$

Hence the classification boundary function of x can be expressed as

$$g(x,\tau) = \sum_{\mathrm{i}=1}^{\mathrm{N}} \alpha_{\mathrm{i}}^* y_{\mathrm{i}} \exp\left(-\frac{\mathrm{kx - DSs_i k^2}}{2\tau^2}\right) + b^* \tag{4.9}$$

where

$$\alpha^* = \arg\max \left[\sum_{\mathrm{i}=1}^{\mathrm{N}} \alpha_{\mathrm{i}} - \frac{1}{2} \sum_{\mathrm{i}=1}^{\mathrm{N}} \sum_{\mathrm{j}=1}^{\mathrm{N}} \alpha_{\mathrm{i}} \alpha_{\mathrm{j}} y_{\mathrm{i}} y_{\mathrm{j}} k(\mathrm{DSs_i}, \mathrm{DSs_j}) \right] \tag{4.10}$$

$$b^* = y_{\mathrm{m}} - \sum_{\mathrm{i}=1}^{\mathrm{N}} \alpha_{\mathrm{i}}^* y_{\mathrm{i}} k(\mathrm{DSs_i}, \mathrm{DSs_m}), \quad \alpha_{\mathrm{m}}^* \neq 0. \tag{4.11}$$

Therefore, for a testing vector x_{s}, the detection method can be determined by

$$x_{\mathrm{s}} \text{ belongs to: } \begin{cases} \mathrm{DSs}^{(-)} \text{ class}, & \text{if } g(x_{\mathrm{s}}, \tau) \leq 0 \\ \mathrm{DSs}^{(+)} \text{ class}, & \text{otherwise} \end{cases}. \tag{4.12}$$

4.2 Classification boundary calculation procedure

To obtain the distribution boundary surrounding a given DSs $\mathrm{DSs}^{(-)}$ with SVM technique, one needs to build another suitable DSs $\mathrm{DSs}^{(+)}$ which is better near or on the distribution boundary $\mathrm{DSs}^{(-)}$. Suppose $\mathrm{DSs}^{(-)} = [\mathrm{T}_{12}, \mathrm{T}_{11}]$, as an example, is a DSs which boundary is to be determined. The data sets $\mathrm{DSs}^{(+)}$ is then generated by following algorithm.

(1). Consider T_{12}, the element of $\mathrm{DSs}^{(-)}$, to follow the normal distribution and calculate its average $\mu_{\mathrm{T}_{12}}$ and standard deviation $\sigma_{\mathrm{T}_{12}}$.

(2). Generate a data set $T_{12}^{(+)}$ based on the normal distribution with parameters $\mu_{\mathrm{T}_{12}^{(+)}} = \mu_{\mathrm{T}_{12}} \pm 10\sigma_{\mathrm{T}_{12}}$ and $\sigma_{\mathrm{T}_{12}^{(+)}} = 8\sigma_{\mathrm{T}_{12}}$. So that there might be around 15% data of $T_{12}^{(+)}$ overlapped on the boundary of data set T_{12}.

(3). Follow the same process to get $T_{11}^{(+)}$. The final data set is obtained as $\mathrm{DSs}^{(+)} = [\mathrm{T}_{12}, \mathrm{T}_{11}]^{(+)}$.

(4). Determine the parameter C in Eq. (4.4). Referring the grid search approach [34],the range of C

$$log_2^{\mathrm{C}} \quad \in \{-5, -4, \ldots, 15\mathrm{g} \tag{4.13}$$

is suggested to be an efficient selection. Based on our numerical testing, we set $C = 2^{15}$.

(5). Determine the parameter τ in Eq. (4.8). Based on Chebyshev's inequality,

$$p(\mathrm{j}x^{(-)} - \mu^{(-)}| \leq \tau) \geq \quad 1 - \frac{(\sigma^{(-)})^2}{\tau^2} \tag{4.14}$$

for any probability distribution, if τ is set at $2\sigma^{(-)}$ to $4\sigma^{(-)}$, there will be at least ($75\% \sim 93.75\%$) samples close to the mean $\mu^{(-)}$. In our grid search approach program, the kernel parameter τ is set as τ 2 $[2\sigma^{(-)}, 4\sigma^{(-)}]$. For each τ, one can obtain a boundary curve $g(x, \tau) = 0$ based on Eq. (4.9).

(6). To obtain the optimal parameter τ^{opt}, based on Eq. (4.12),the classification accuracy (CA) for the learning DSs $[T_{12}, T_{11}]$ and $[T_{12}, T_{11}]^{(+)}$ at

τ 2 $[2\sigma^{(-)}, 4\sigma^{(-)}]$ is calculated by

$$CA(\%) = \frac{\mathrm{TP+TN}}{\mathrm{TP+FP+FN+TN}} \quad , \tag{4.15}$$

where TP represents true $[T_{12}, T_{11}]$, TN represents true $[T_{12}, T_{11}]^{(+)}$, FP represents false $[T_{12}, T_{11}]$ and FN represents false $[T_{12}, T_{11}]^{(+)}$. The τ corresponding to the maximum of CA is selected as $\tau = \tau^{\mathrm{opt}}$.

(7). The classification boundary function $g(x, \tau^{\mathrm{opt}}) = 0$ is then obtained by substituting $\tau = \tau^{\mathrm{opt}}$ to Eq. (4.9).

4.3 Experimental results

The total DSs including 242 normal sound samples (denoted as $\mathrm{DSs_T^{NM}}$ consisting of T_{12} and T_{11}, and $\mathrm{DSs_F^{NM}}$ consisting of F_{G} and F_{W}) from 46 healthy persons and 226 VSD sound samples ($\mathrm{DSs_T^{VSD}}$ and $\mathrm{DSs_F^{VSD}}$) including 62 SVSD sound samples ($\mathrm{DSs_T^{SVSD}}$ and $\mathrm{DSs_F^{SVSD}}$ from 10 patients), 90 MVSD sound samples ($\mathrm{DSs_T^{MVSD}}$ and $\mathrm{DSs_F^{MVSD}}$ from 15 patients) and 74 LVSD sound samples ($\mathrm{DSs_T^{LVSD}}$ and $\mathrm{DSs_F^{LVSD}}$ from 12 patients) ($\mathrm{DSs_T^{VSD}}$ and $\mathrm{DSs_F^{VSD}}$) are used to obtain the classification boundary functions. Firstly, the 80% DSs are randomly selected from the total DSs to generate the boundary curves $g_{\mathrm{T}}^{\mathrm{NM}} = 0$ and $g_{\mathrm{F}}^{\mathrm{NM}} = 0$ for normal sounds, $g_{\mathrm{T}}^{\mathrm{VSD}} = 0$ and $g_{\mathrm{F}}^{\mathrm{VSD}} = 0$ for VSD sounds. Further, in order to reduce the influence due to selection of the training data samples, the boundary curves were calculated by three times randomly selected data samples. The results have shown that there is not big difference between the obtained three boundary curves. The boundary curves shown in Figure 4.2 are the averaged curves. Based on Eq. (4.12), by the

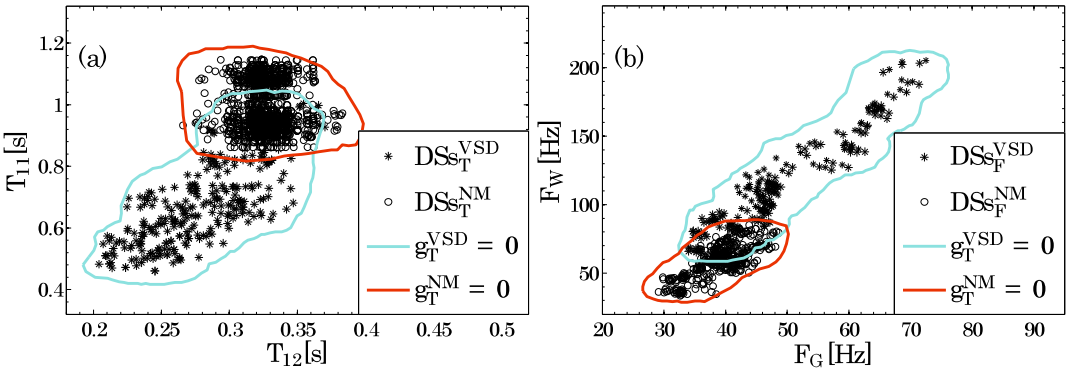

Figure 4.2 Experimental results of the classifiers designed for identification of normal and VSD sounds.

features $[T_{12}, T_{11}]$ and $[F_G, F_W]$ to detect sound for identifying VSD sounds and normal sound, the classification labelings in the time domain (CL_T) and in the frequency domain (CL_F) are introduced as follows:

$$CL_T = \begin{cases} 1, & \text{if } g_T^{VSD} \le 0 \text{ and } g_T^{NM} > 0 \\ 0, & \text{if } g_T^{VSD} \le 0 \text{ and } g_T^{NM} \le 0 \\ -1, & \text{if } g_T^{VSD} > 0 \text{ and } g_T^{NM} \le 0 \\ NaN, & \text{if } g_T^{VSD} > 0 \text{ and } g_T^{NM} > 0 \end{cases} \tag{4.16}$$

$$CL_F = \begin{cases} 1, & \text{if } g_F^{VSD} \le 0 \text{ and } g_F^{NM} > 0 \\ 0, & \text{if } g_F^{VSD} \le 0 \text{ and } g_F^{NM} \le 0 \\ -1, & \text{if } g_F^{VSD} > 0 \text{ and } g_F^{NM} \le 0 \\ NaN, & \text{if } g_F^{VSD} > 0 \text{ and } g_F^{NM} > 0 \end{cases} \tag{4.17}$$

Table 4.1
Confusion matrix representation

Actual	Predicted	
	Positive	Negative
Positive	True Positive (TP)	False Negative (FN)
Negative	False Positive (FP)	True Negative (TN)

Finally, the detection index (DI) for identifying VSD by heart sound feature parameters is defined by

$$\mathrm{DI} = \mathrm{CL_T} + \mathrm{CL_F} \begin{cases} \geq 1, & \text{VSD} \\ = 0, & \text{Not Sure} \\ \leq -1, & \text{Normal} \\ = NaN, & \text{Others} \end{cases} \tag{4.18}$$

To evaluate the performance of these classification boundary curves, by the detection index Eq. (5.17) and the elements of the confusion matrix Table 4.1, classification accuracy (CA), sensitivity (Se) and specificity (Sp) value can be defined as

$$\begin{cases} CA(\%) = \frac{\mathrm{TP+TN}}{\mathrm{TP+FP+FN+TN}} \times 100 \\ Se(\%) = \frac{\mathrm{TP}}{\mathrm{TP+FN}} \times 100 \\ Sp(\%) = \frac{\mathrm{TN}}{\mathrm{FP+TN}} \times 100 \end{cases}, \tag{4.19}$$

where TP represents true VSD sound, TN represents true normal sound, FP represents false VSD sound and FN represents false normal sound. Using the

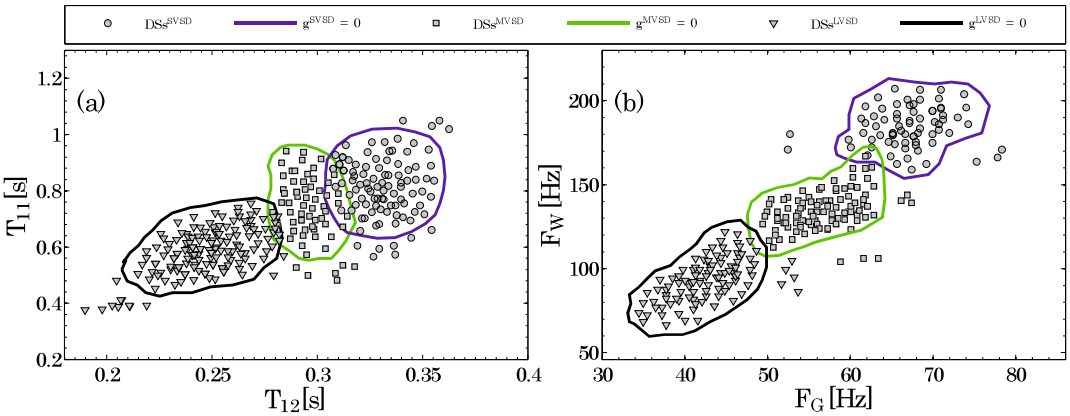

Figure 4.3 Classification boundaries and the feature parameters extracted from SVSD,MVSD and LVSD sounds.

classification boundaries to detect a new DSs consisting of 253 normal and 124 VSD sounds, our study [38] showed that the sensitivity Se was 98.8%, the specification Sp was 98.1% and the accuracy CA was 98.4%.

Since the VSD sounds consists of the SVSD, MVSD and LVSD, In this section, 62 SVSD sound samples, 90 MVSD sound samples and 74 LVSD sound samples are used to obtain the boundary curves for SVSD, MVSD and LVSD. The boundary curves were calculated by three times randomly selected data samples. The results have shown that there is not big difference between the obtained three boundary curves. The boundary curves shown in Figure 4.3 were the averaged curves.

Finally, a new data set, in which 253 normal and 124 VSD (56 SVSD, 30 MVSD, and 38 LVSD) sounds were consisted, are additionally examined by the proposed method the new sounds were used for detection. The accuracies Se, Sp and CA are summarized in Table 4.2.

Table 4.2
Classification accuracies for SVSD, MVSD and LVSD

Accuracies	VSD(350)		
	SVSD(118)	MVSD(120)	LVSD(112)
Se(%)	95.2	94.6	94.9
Sp(%)	94.2	93.1	93.6
CA(%)	94.8	93.7	94.1

4.4 Summary

This section proposed how to build the classification boundary curves as classifier to diagnose VSD and NM sounds. To obtain the distribution boundary surrounding a given DSs $DSs^{(-)}$ with SVM technique, based on the mean value ($\mu^{(-)}$) and standard deviation ($\sigma^{(-)}$) of the given $DSs^{(-)}$, another suitable DSs $DSs^{(+)}$ which was better near or on the distribution boundary $^{(-)}$ was generated firstly. The radio basis function(RBF) was used as kernel function and the parameter τ was set at $2\sigma^{(-)}$ to $4\sigma^{(-)}$, and then the max classification accuracy was used to determine the optimal τ and obtained the classification boundary curve. The accuracies Se, Sp, CA for diagnosing VSD form NM sounds were 98.8%, 98.1% and 98.4%. Since VSD can be divided into three types SVSD, MVSD and LVSD, the same method was used to obtain the classification boundary curves for SVSD, MVSD and LVSD. The accuracies Se, Sp, CA for diagnosing SVSD, MVSD, and LVSD were shown in Table 4.2. Although the classification boundary curves (Figure 4.2 and Figure 4.3) for a training data sets(DSs) were obtained with higher accuracies by SVM technique, the mathematical expressions of the classification curves were too complicated to be expressed by parameters. Furthermore, the computation was so huge. To simplify the mathematical expressions of the classification curves

to reduce the computation, the models for the classification boundary curves were considered in the next chapter.

Chapter 5

HSs Detection System

5.1 Classification model procedure

In the above section, although the classification boundary curves plotted in Figure 4.2 and Figure 4.3 for a training data sets (DSs) were obtained with higher accuracies by SVM technique, the mathematical expressions of the classification curves were too complicated to be expressed by parameters. Furthermore, the computation was so huge. To simplify the mathematical expressions of the classification curves to reduce the computation, the models for the classification boundary curves were considered. Since the shapes of classification boundary curves plotted in Figure 4.2 and Figure 4.3 were similar to the ellipses, the ellipse models (EMs) for the classification boundary curves are built in this section.

Ellipse fitting based on least squares method is widely used [68; 69; 70; 71; 72; 73; 74; 75; 76]. It is an optimal estimation technology introduced by the maximum likelihood when the random error is assumed to belong to normal distribution, and it can minimize the error of measurement. Therefore, it can also be seen

as a group from measured value and a group of unknown variables method. An ellipse is a special case of the general conic which can be described by an implicit second order polynomial

$$F(A, x, y) = A_{11}x^2 + A_{21}xy + A_{31}y^2 + A_{41}x + A_{51}y + A_{61} = 0 \tag{5.1}$$

with an ellipse specific constraint

$$A_{21}^2 - 4A_{11}A_{31} \leq 0 \tag{5.2}$$

where $A_{1i}(i = 1, 2, ..., 6)$ are coefficients of the ellipse, and (x, y) are coordinates of points lying on it. The polynomial $F(A, x, y)$ is called the algebraic distance of the point (x, y) to the given conic. Based on least square method, the fitting of a general conic to a set of points $(x_i, y_i), i = 1, c, N$ may be approach by minimizing the sum of square algebraic distances of the points to the conic which is represented by coefficient A:

$$\min_{A} \sum_{i=1}^{N} F^2(A, x_i, y_i) \tag{5.3}$$

which can be solved directly by least square approach. In this paper, to describe the significance of the ellipse model for the classification boundary curves, the ellipse as shown in Figure 5.1 is presented by geometric parameters $[x_c, y_c, a, b, \theta]$, where the point $[x_c, y_c]$ is the center, a is the semi-major length, b is the semi-minor length, and θ is the counterclockwise angle of rotation from the x-axis and the major axis of the ellipse. The $[x_c, y_c, a, b, \theta]$ corresponding to the ellipse in Eq. (5.1) is transformed by

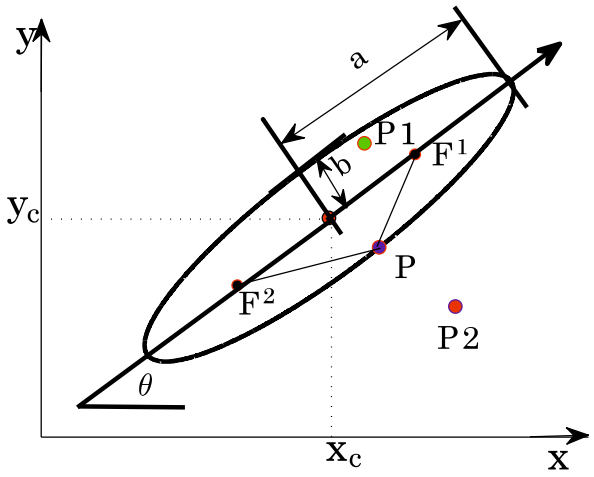

Figure 5.1 Ellipse geometric representation in the x-y axis plane

$$x_c = \frac{A_{21}A_{51} - 2A_{31}A_{41}}{4A_{11}A_{31} - A_{21}^2} \tag{5.4}$$

$$y_c = \frac{A_{21}A_{41} - 2A_{11}A_{51}}{4A_{11}A_{31} - A_{21}^2} \tag{5.5}$$

$$a = \frac{\sqrt{2(A_{11}A_{51}^2 + A_{31}A_{41} + A_{21}^2A_{61} - A_{21}A_{41}A_{51} - 4A_{11}A_{31}A_{61})}}{(A_{21}^2 - 4A_{11}A_{31})\left[\sqrt{(A_{11} - A_{31})^2 + A_{21}^2} - A_{11} - A_{31}\right]} \tag{5.6}$$

$$b = \frac{\sqrt{2(A_{11}A_{51}^2 + A_{31}A_{41} + A_{21}^2A_{61} - A_{21}A_{41}A_{51} - 4A_{11}A_{31}A_{61})}}{(A_{21}^2 - 4A_{11}A_{31})\left[-\sqrt{(A_{11} - A_{31})^2 + A_{21}^2} - A_{11} - A_{31}\right]} \tag{5.7}$$

$$\theta = \begin{cases} 0 & \text{for} \quad A_{21} = 0 \quad \text{and} \quad A_{11} \leq A_{31} \\ \frac{\pi}{2} & \text{for} \quad A_{21} = 0 \quad \text{and} \quad A_{11} > A_{31} \\ \operatorname{arccot}(\frac{A_{11}-A_{31}}{A_{21}})/2 & \text{for} \quad A_{11} > A_{31} \quad \text{and} \quad A_{21} \neq 0 \\ \frac{\pi}{2} + \operatorname{arccot}(\frac{A_{11}-A_{31}}{A_{21}})/2 & \text{for} \quad A_{31} > A_{11} \quad \text{and} \quad A_{21} \neq 0 \end{cases} \tag{5.8}$$

Therefor, for the points like P on the ellipse, P1 within the ellipse and P2 outside of the ellipse in Figure 5.1, according to the definition of ellipse, the points P, P1 and P2 must be satisfied with

$$\begin{cases} \mathrm{j}\ P - F^1\ \mathrm{j} + \mathrm{j}\ P - F^2\ \mathrm{j} = 2a \\ \mathrm{j}\ P1 - F^1\ \mathrm{j} + \mathrm{j}\ P1 - F^2\ \mathrm{j} < 2a \\ \mathrm{j}\ P2 - F^1\ \mathrm{j} + \mathrm{j}\ P2 - F^2\ \mathrm{j} > 2a \end{cases} \tag{5.9}$$

where F^1 and F^2 are the focus points are computed by

$$\begin{cases} F^1 : (x_c + \sqrt{a^2 - b^2}\cos(\theta), y_c + \sqrt{a^2 - b^2}\sin(\theta)) \\ F^2 : (x_c - \sqrt{a^2 - b^2}\cos(\theta), F_c - \sqrt{a^2 - b^2}\sin(\theta)) \end{cases} \tag{5.10}$$

5.2 Ellipse results

Based on the classification boundary curves shown in Figure 4.2, the EMs are plotted in Figure 5.2. The geometrical model parameters of the EM, which are denoted as $[x_c, y_c, a, b, \theta]$, are [0.326, 0.9985, 0.1878, 0.0689, 85.69°] and [0.290, 0.7196, 0.0655, 0.3166, 80.3474°] for NM and VSD in time-domain. In frequency-domain they are [38.7042, 59.2052, 32.046, 8.6774, 76.39°] and [54.38, 135.28,

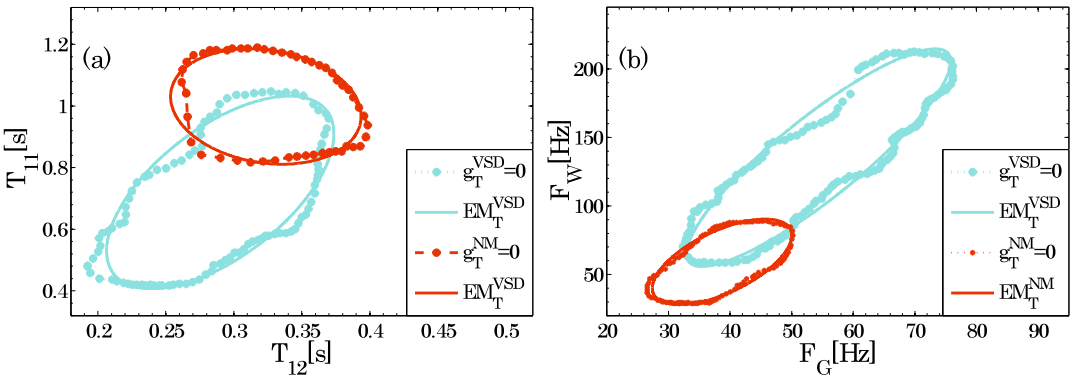

Figure 5.2 The classification boundary curves and their ellipse models for normal sounds and VSD sounds. (a) in the time domain and (b) in the frequency domain

81.68, 9.80,76.39°]. Therefore, by $[x_c, y_c, a, b, \theta]$ we can determine the distribution of the diagnostic features T_{12}, T_{11}, F_G, and F_W. Furthermore, the angle perhaps indicates an pertinence relation between T_{12} and T_{11} in time-domain, and between F_G and F_W in frequency-domain. Based on those classification boundary curves shown in Figure 4.3, the EMs are plotted in Figure 5.3. The geometrical model parameters of the EMs, which are denoted as $[x_c, y_c, a, b, \theta]$, are [0.324, 0.825, 0.198, 0.021, 90.6°], [0.296, 0.757, 0.211, 0.020, 90.9°], and [0.247, 0.597, 0.171, 0.036, 84.7°] for SVSD, MVSD, and LVSD in T_{12}-T_{11} domain, and in frequency-domain they are [67.25, 185.49, 28.67, 8.52, 85.7°], [55.08, 132.54, 32.39, 10.07, 76.5°], and [41.99, 91.82, 33.58, 6.83,81.29°], respectively.

5.3 Ellipse models based diagnostic method

The ellipse models are built for the boundary curves obtained for NM and VSD (SVSD, MVSD and LVSD) to diagnose the NM and VSD (SVSD, MVSD, and LVSD). Actually, using the ellipse models to diagnose the heart sounds is to

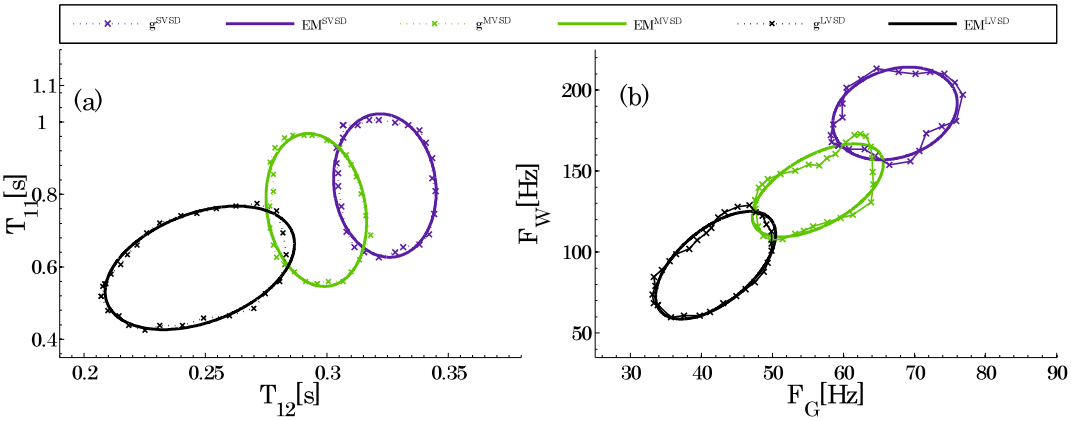

Figure 5.3 The classification boundary curves and their ellipse models. (a) in the time domain and (b) in the frequency domain

judge whether the $[T_{12}, T_{11}]$ and $[F_{\mathrm{G}}, F_{\mathrm{W}}]$ are both distributed into the insides of the ellipse models for NM or VSD(SVSD, MVSD, LVSD). According to the relationship between the points and the ellipse using the ellipse definition, the numerical discrimination results denoted as $\mathrm{NDR}_{\mathrm{T}}^{\mathrm{NM}}$, $\mathrm{NDR}_{\mathrm{T}}^{\mathrm{SVSD}}$, $\mathrm{NDR}_{\mathrm{T}}^{\mathrm{MVSD}}$ and $\mathrm{NDR}_{\mathrm{T}}^{\mathrm{LVSD}}$ in time-domain, and $\mathrm{NDR}_{\mathrm{F}}^{\mathrm{NM}}$, $\mathrm{NDR}_{\mathrm{T}}^{\mathrm{SVSD}}$, $\mathrm{NDR}_{\mathrm{F}}^{\mathrm{MVSD}}$ and $\mathrm{NDR}_{\mathrm{F}}^{\mathrm{LVSD}}$ in frequency-domain are determined as follow.

Suppose the points $P_{\mathrm{T}}(T_{12}, T_{11})$ and $P_{\mathrm{F}}(F_{\mathrm{G}}, F_{\mathrm{W}})$ are extracted from one heart sound. Here the ellipse models of MVSD are taken as the examples to check the $P_{\mathrm{T}}(T_{12}, T_{11})$ and $P_{\mathrm{F}}(F_{\mathrm{G}}, F_{\mathrm{W}})$ whether they are inside the ellipse models (Figure 5.4), according to the ellipse definition and classification, the $\mathrm{NDR}_{\mathrm{T}}^{\mathrm{MVSD}}(P_{\mathrm{T}})$ can be defined as

$$\mathrm{NDR}_{\mathrm{T}}^{\mathrm{MVSD}}(P_{\mathrm{T}}) = \begin{cases} 1 & \text{if} \quad \mathrm{j}\, P_{\mathrm{T}} - F1\,\mathrm{j} + \mathrm{j}\, P_{\mathrm{T}} - F2\,| \leq 2a_{\mathrm{T}} \\ -1 & \text{if} \quad \mathrm{j}\, P_{\mathrm{T}} - F1\,\mathrm{j} + \mathrm{j}\, P_{\mathrm{T}} - F2\,\mathrm{j} > 2a_{\mathrm{T}} \end{cases} \tag{5.11}$$

where F1 and F2 are the focus of the ellipse model $\mathrm{EM}_{\mathrm{T}}^{\mathrm{MVSD}}$ plotted in Figure

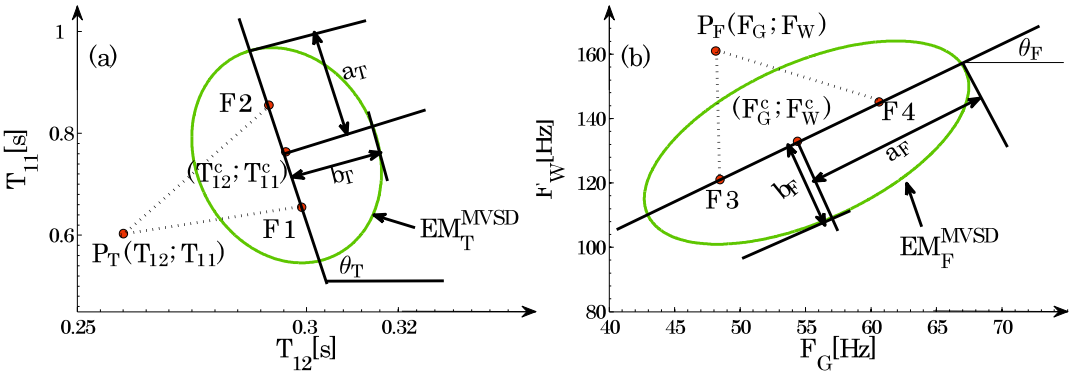

Figure 5.4 The example for MVSD ellipse model. (a) in the time domain and (b) in the frequency domain

5.4 (a) and computed by the center (T^c_{12}, T^c_{11}), the semi-major axis (a_T) and the semi-minor axis (b_T) of the ellipse model EM^{MVSD}_T as

$$F1 : (T_{12} + \sqrt{a_T^2 - b_T^2}\cos(\theta_T), T_{11} + \sqrt{a_T^2 - b_T^2}\sin(\theta_T)) \tag{5.12}$$

$$F2 : (T_{12} - \sqrt{a_T^2 - b_T^2}\cos(\theta_T), T_{11} - \sqrt{a_T^2 - b_T^2}\sin(\theta_T)) \tag{5.13}$$

, and the $NDR^{MVSD}_F(P_F)$ can be defined as

$$NDR^{MVSD}_F(P_F) = \begin{cases} 1 & \text{if} \quad |P_F - F3| + |P_F - F4| \leq 2a_F \\ -1 & \text{if} \quad |P_F - F3| + |P_T - F4| > 2a_F \end{cases} \tag{5.14}$$

where F3 and F4 are the focus of the ellipse model EM^{MVSD}_F plotted in Figure 5.4 (b) and computed by the center (F^c_G, F^c_W), the semi-major axis (a_F) and the semi-minor axis (b_F) of the ellipse model EM^{MVSD}_F as

$$F3 : (F_G + \sqrt{a_F^2 - b_F^2}\cos(\theta_F), F_W + \sqrt{a_F^2 - b_F^2}\sin(\theta_F)) \tag{5.15}$$

$$F4 : (F_G - \sqrt{a_F^2 - b_F^2}\cos(\theta_F), F_W - \sqrt{a_F^2 - b_F^2}\sin(\theta_F)) \tag{5.16}$$

In the same way, the $NDR_T^{NM}(P_T)$, $NDR_T^{SVSD}(P_T)$ and $NDR_T^{LVSD}(P_T)$ of the point P_T in ellipses in time-domain can be determined, and the $NDR_F^{NM}(P_F)$, $NDR_F^{SVSD}(P_F)$, $NDR_F^{LVSD}(P_F)$, $NDR_F^{LVSD}(P_F)$ of the point P_F in ellipses in frequency-domain can be determined. The detection result (DR) for identifying heart sounds by P_T and P_F is defined by

$$DR: \begin{cases} NM & \text{for } NDR_T^{NM} + NDR_F^{NM} = 2 \\ VSD & \text{for } NDR_T^{VSD} + NDR_F^{VSD} = 2 \\ SVSD & \text{for } NDR_T^{SVSD} + NDR_F^{SVSD} = 2 \\ MVSD & \text{for } NDR_T^{MVSD} + NDR_F^{MVSD} = 2 \\ LVSD & \text{for } NDR_T^{LVSD} + NDR_F^{LVSD} = 2 \end{cases} . \quad (5.17)$$

Table 5.1
Comparative analysis for classification accuracies by the EMs and boundary curves

Accuracies	Boundaries	EMs
Se(%)	98.8	98.6
Sp(%)	98.1	98.4
CA(%)	98.4	98.5

Table 5.2
Comparative analysis for classification accuracies for SVSD, MVSD and LVSD by EMs and Boundary curves

Accuracies	SVSD		MVSD		LVSD	
	Boundaries	EMs	Boundaries	EMs	Boundaries	EMs
Se(%)	95.2	95.4	94.6	95.1	94.9	95.1
Sp(%)	94.2	95.8	93.1	94.2	93.6	94.8
CA(%)	94.8	95.7	93.7	94.7	94.1	95.0

5.4 Experimental analysis

By these EMs and the boundary curves obtained in the the section 4.3 to detect the same DSs (NM(475), SVSD(118), MVSD(120) and LVSD(112)) used in the section 4.3, the comparative accuracy results for NM and VSD sounds are showed in Table 5.1. The comparative accuracy results for SVSD, MVSD and LVSD are shown in Table 5.2.

From the comparative analysis results (Table 5.1 and Table 5.2), the results show that

(1). The Table 5.1 shows that the accuracy results for NM and VSD are not obvious different between using ellipse models and boundary curves.

(2). The Table 5.2 shows that the performance of ellipse models seems to be a little better than of boundary curves.

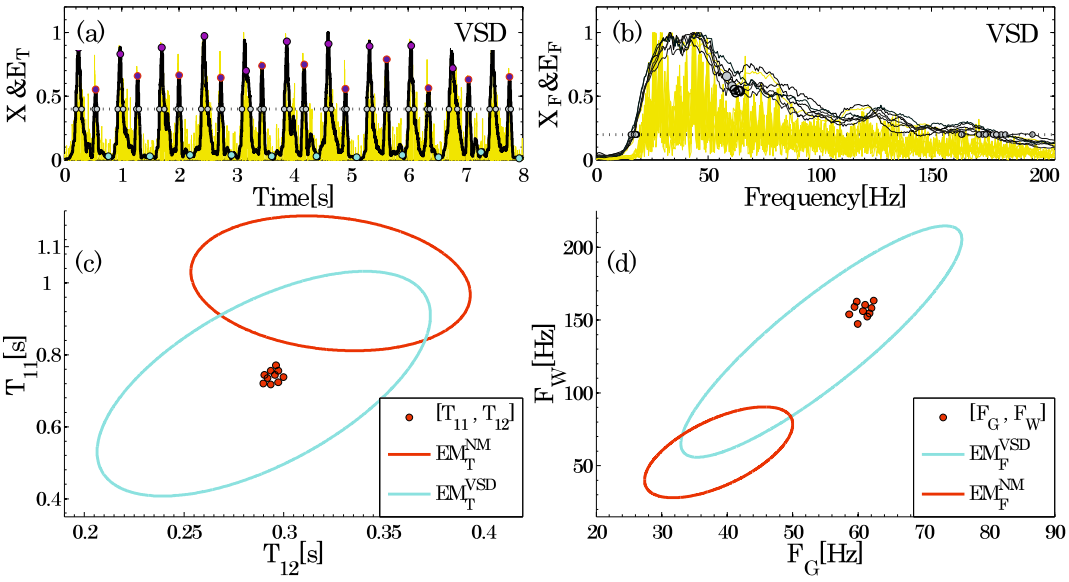

Figure 5.5 The examples for heart sounds detection procedure. (a) The envelope EM_T and (b) the envelope EM_F of the VSD. The corresponding diagnostic graphics representations of $[T_{12}; T_{11}]$ obtained from VSD at H_T = 0:4 are displayed in (c) and $[F_G; F_W]$ obtained from VSD at H_F = 0:2 are shown in (d).

Therefore, the ellipse models can replace the boundary curves to diagnose the heart sounds.

To explain this detection procedure much better, the VSD sounds and normal sounds (NM)are taken as the examples to be analyzed (Figure 5.5 and Figure 5.6). Figure 5.5 shows the example which signal is collected from a female patient (Φ=12 mm) of age 2 with 12 kg. For the VSD sound, the threshold values H_T and H_F are set manually at 0.4 and 0.2 in order to obtain a reasonable set of the diagnostic parameters $[T_{12}, T_{11}]$ and $[F_G, F_W]$ (Figure 5.5 a and b). Figure 5.5 (c) and (d) show the corresponding diagnostic scatter grams. It is obvious that the plots of the parameters $[T_{12}, T_{11}]$s and $[F_G, F_W]$s are both concentrated into the ellipse model of MVSD. Therefore the VSD case might be discriminated as MVSD, and the diagnostic result is corresponding to the clinical diagnosis because

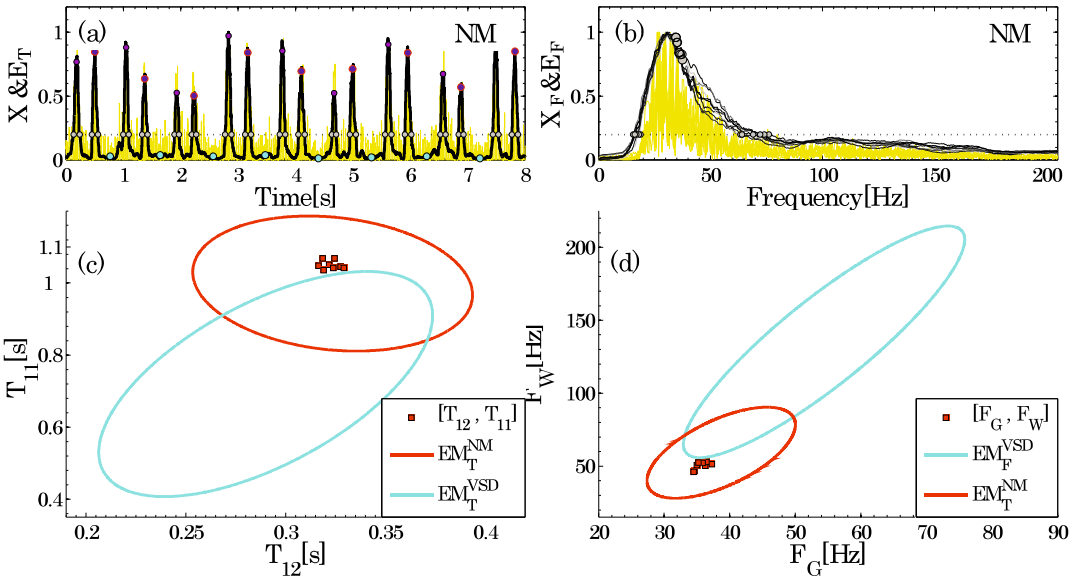

Figure 5.6 The examples for heart sounds detection procedure. (a) The envelope EM_T and (b) the envelope EM_F of the NM. The corresponding diagnostic graphics representations of $[T_{12}; T_{11}]$ obtained from VSD at H_T = 0:2 are displayed in (c) and $[F_G; F_W]$ obtained from VSD at H_F = 0:2 are shown in (d).

Φ of it is 12mm. Figure 5.6 shows the example, which signal is collected from a healthy woman of age 22 with weight 49 kg. For NM, to obtain a reasonable set of the diagnostic parameters $[T_{12}, T_{11}]$ and $[F_G, F_W]$ (Figure 5.6(c) and (d)), the threshold values H_T and H_F are set manually at 0.2. The corresponding diagnostic scatter grams are shown in Figure 5.6 (c) and (d). It is obvious that the plots of the parameters $[T_{12}, T_{11}]$ and $[F_G, F_W]$ are both concentrated into the ellipse model of NM. Therefore the VSD case might be discriminated as NM. Therefore, this detection system can easily help the user to understand the detecting heart sound from in-time domain and in frequency-domain.

5.5 HSs diagnostic results for clinical sounds

To evaluate the efficiency of the proposed method, besides NM sounds from three healthy males in yamaguchi university and two females in xihua university and VSD sounds from patients only with VSD in department of cardiology surgery of Chengdu military general hospital of PLA, an AR, an AF, an AS, and a MS sounds are randomly selected to be diagnosed. The VSD sounds include two LVSD sounds, which are from a female patient of age 6 with weight 32 kg (named LVSD1 (Φ = 21 mm)) and a male of age 4 with weight 19 kg (LVSD2 (Φ = 17 mm)); three MVSD sounds which are from a female of age 2 with weight 15 kg (MVSD1(Φ = 14 mm)), a female of age 2 with weight 15 kg (MVSD2 (Φ = 10 mm)) , and a female of age 2 with weight 15 kg (MVSD3 (Φ = 6 mm)); two SVSD sounds, which are from a female patient of age 6 with weight 32 kg (SVSD1 (Φ = 5 mm)) and a male of age 4 with weight 19 kg (SVSD2 (Φ = 5 mm)). The four normal sounds are collected from a female of age 23 with weight 56 kg (NM1), a male of age 22 with weight 68 kg (NM2), a male of age 27 with weight 75 kg (NM3), and a healthy male of age 18 with weight 70 kg (NM4). The AR, AF, AS, and MS sounds collected from an online clinical training web site are denoted AR, AF, AS, and MS, respectively. The features extracted from LVSD1, LVSD2, MVSD1, MVSD2, MVSD3, SVSD1, SVSD2, NM1, NM2, NM3, NM4, AR, AF, AS, and MS are shown in Figure 5.7, and the sound discrimination results are shown as Table 5.3. Here, MVSD1 is taken as an example to introduce the performance using $[T_{12}, T_{11}]$ and $[F_{\mathrm{G}}, F_{\mathrm{W}}]$; the results of MVSD1 in Figure 5.7

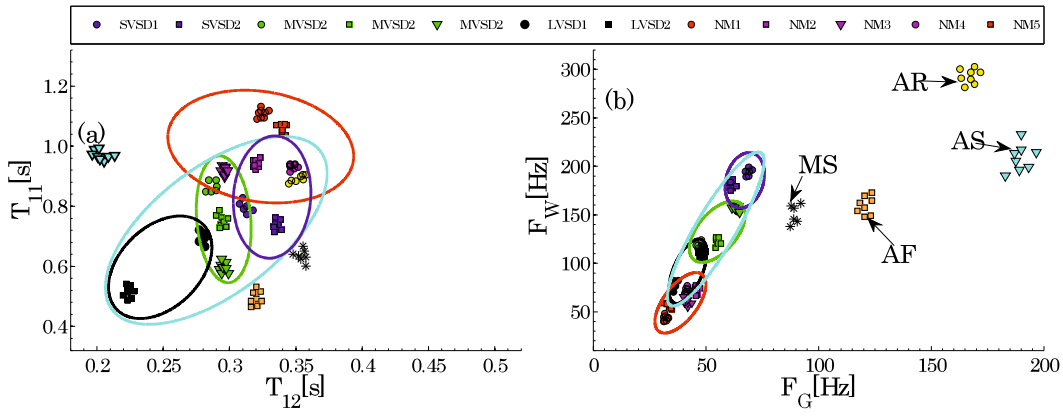

Figure 5.7 Classification models and the distribution of heart sound feature parameters.

Table 5.3
Discrimination results by the numerical discrimination results

HS	NM		VSD		LVSD		MVSD		SVSD		DR
	NDR_T	NDR_F	NDR_T	NDR_F	NDR_T	NDR_F	NDR_T	NDR_F	DNR_T	NDR_F	
LVSD1(Φ = 21 mm)	-1	-1	1	1	1	1	-1	1	-1	-1	VSD:LVSD
LVSD2(Φ = 17 mm)	-1	1	1	1	1	1	1	-1	-1	-1	VSD:LVSD
MVSD1(Φ = 14 mm)	1	-1	1	1	-1	1	1	1	-1	-1	VSD:MVSD
MVSD2(Φ = 10 mm)	-1	-1	1	1	-1	-1	1	1	-1	-1	VSD:MVSD
MVSD3(Φ = 7 mm)	-1	-1	1	1	-1	-1	1	1	-1	1	VSD:MVSD
SVSD1(Φ = 5 mm)	-1	-1	1	1	-1	-1	1	-1	1	1	VSD:SVSD
SVSD2(Φ = 5 mm)	-1	-1	1	1	-1	-1	-1	-1	1	1	VSD:SVSD
NM1	1	1	-1	-1	-1	-1	-1	-1	-1	-1	NM
NM2	1	1	1	1	-1	1	-1	-1	1	-1	NM:VSD
NM3	1	1	1	1	-1	-1	-1	-1	1	-1	NM:VSD
NM4	1	1	1	-1	-1	-1	1	-1	-1	-1	NM
AF	-1	-1	-1	-1	-1	-1	-1	-1	-1	-1	-
AR	1	-1	1	-1	-1	-1	-1	-1	1	-1	-
AS	-1	-1	-1	-1	-1	-1	-1	-1	-1	-1	-
MS	-1	-1	-1	-1	-1	-1	-1	-1	-1	-1	-

show that

$$\text{MVSD1}: \begin{cases} \text{the plots of } [T_{12}, T_{11}] \text{ are distributed within: VSD, MVSD, and NM} \\ \text{the plots of } [F_{\mathrm{G}}, F_{\mathrm{W}}] \text{ are distributed within: VSD, MVSD and LVSD} \end{cases} . \tag{5.18}$$

Therefore, MVSD1 might be diagnosed as in the NM, VSD and MVSD classes using only $[T_{12}, T_{11}]$, and only using $[F_{\mathrm{G}}, F_{\mathrm{W}}]$ it might be diagnosed as the VSD, LVSD and MVSD classes. However, using $[T_{12}, T_{11}]$ and $[F_{\mathrm{G}}, F_{\mathrm{W}}]$ it might be diagnosed as VSD and MVSD, which corresponds to the clinical diagnosis and its detection results denoted as VSD:MVSD, shown in Table 5.3. Of course, sound is very difficult to be diagnosed, and problems will occur in this detection system, like for NM2. The results of NM2 in Figure 5.7 show that

$$\text{NM2}: \begin{cases} \text{the plots of } [T_{12}, T_{11}] \text{ are distributed within: NM, VSD and SVSD} \\ \text{the plots of } [F_{\mathrm{G}}, F_{\mathrm{W}}] \text{ are distributed within: NM, VSD and LVSD} \end{cases} . \tag{5.19}$$

Therefore, NM2 might be diagnosed as in the NM and VSD classes (denoted as NM:VSD), which is in keeping with the diagnosis result that the classification accuracy between NM and VSD is 98.4% not 100%. Similarly, the detection results corresponding to Figure 5.7 are summarized in Table 5.3. Furthermore, the analysis results for the typical clinical AR, AS, MR, AF sounds plotted in Figure 5.7 show that they are easy to diagnose, and are not mistaken as NM or VSD sounds, which are contrary to the results that the VSD was incorrectly classified as aortic stenosis (AS) or aortic regurgitation (AR), as summarized in

[77]. Therefore, the proposed method might be efficient to discriminate VSD sounds.

5.6 Summary

This section proposed how to build the classification model as classifier to diagnose VSD (LVSD, MVSD, SVSD) and NM sounds. Firstly, according to an implicit second order polynomial of the ellipse ($F(A, x, y) = A_{11}x^2 + A_{21}xy + A_{31}y^2 + A_{41}x + A_{51}y + A_{61} = 0$), the ellipse models were obtained to fit the boundary curves by the least squares method. The ellipse models were expressed by the parameters $[a, b, x_c, y_c, \theta]$. And then according to the relationship between the points and the ellipse using the ellipse definition, the numerical discrimination results denoted as NDR_T^{NM}, NDR_T^{SVSD}, NDR_T^{MVSD} and NDR_T^{LVSD} in time-domain, and NDR_F^{NM}, NDR_T^{SVSD}, NDR_F^{MVSD} and NDR_F^{LVSD} in frequency-domain were determined. Based on these numerical discrimination results, The detection result (DR) for identifying heart sounds were defined. Finally, By comparing analysis of the accuracies Se, Sp, CA between using boundary curves and the ellipse models to clarify the efficient of using ellipse models to detect heart sound, and by comparing analysis the results in the Table 5.1 with the results in the Table 5.2, the ellipse models can replace the boundary curves to diagnose the heart sounds.

Chapter 6

Conclusions

In recent years, many great achievements in diagnosing heart diseases using heart sounds analysis, which is the simplest and cheapest method to noninvasively diagnose heart diseases, were proposed. However, to date, there was not an entire practical diagnosis system helping an inexperienced or non-clinical experience person to detect heart disease with the simple method. Furthermore, because the different sizes of VSD compared to normal sound showed the different distribution characteristics between in the time domain and in the frequency domain, VSD was reported to be difficultly discriminated from normal sounds or other typical heart murmurs, and still less the different sizes of VSD diagnosis. To overcome these problems, a high accuracy numerical diagnostic system for diagnosing the different sizes of VSD, which correspond to the different treatments for recovering VSD, was proposed. The innovation of this thesis could be listed as follows:

- The diagnostic features, which were the critical factors for ensuring the heart disease diagnosis system with high-efficiency, were extracted from the heart sound.
- Boundary curves based on support vector machines (SVM) were proposed

to used as classifiers to diagnosis VSD.

- Boundary curves models-based a high-efficient numerical diagnostic system for diagnosing the different sizes of VSD was carried out.

To extract the high-efficient diagnostic features, the distribution characteristic for the typical different sizes of VSD sound in the time domain and the frequency domain is summarized. According to the distribution characteristics of VSD, the time domain features and frequency domain features were considered. Referring to the diagnostic features definition method in our previous studies combined with the distribution characteristic of VSD sounds, based on a novel method MWHT, which is proposed as a novel automatic heart sound segmentation method without any amplitude threshold value and having higher performance than other segmentation methods, the high-efficient diagnostic features $[T_{12}, T_{11}]$ in the time domain and $[F_{\mathrm{G}}, F_{\mathrm{W}}]$ in the frequency domain are proposed, and the efficiency of the features had been convinced using the statistic features of the diagnostic features. These contents were detailed in chapter 3.

To evaluate the performance of the proposed diagnostic features, an boundary curve algorithm based on SVM, which was used successfully for many problems including heart murmurs classification, cancer diagnosis, etc, was proposed to surround a given datasets with high accuracy and was detailed in chapter 4. The chapter 4 includes:

- To use SVM technique to generate a suitable boundary curve for a given datasets, how to generate another suitable datasets which is near to or on the distribution of the given datasets, was proposed.

- According to the given datasets, the range for the parameter of the function used as the kernel function of SVM was defined.
- According to the classification accuracy, how to automatically search the optimal parameter to generate a suitable boundary curve as classifier was proposed.
- The performance of proposed boundary curves was evaluated by clinical heart sounds.

To build a high-efficient diagnostic system for diagnosing the different sizes of VSD by the diagnostic features. The contents of chapter 5 could be summarized in the following.

- According to the shapes of boundary curves, the ellipse models are proposed.
- The Feasibility of using ellipse models to replace boundary curves was discussed using the classification accuracy of classifying the same datasets.
- To reduce the diagnosis error produced by observation, according to the function of ellipse models and the signification of classification. A numerical diagnostic system for diagnosing the different sizes of VSD was carried out.

To validate the usefulness of the proposed numerical diagnosis system for detecting sounds besides clinical different sizes of VSD and normal sounds, 4 types common heart diseases which are aortic regurgitation (AR), atrical fibrillation (AF), aortic stenosis (AS) and mitral stenosis (MS) sounds are used as examples to be detected, and the performance using the accuracies is summarized. The

results showed that the proposed method perhaps provided an efficient way to obtain the efficient range of features which characterized different types of heart murmurs.

Acknowledgements

I would never have been able to finish my dissertation without the guidance of my thesis advisor professor, help from friends, and support from my family and wife.

In the first place I would like to record my gratitude to my advisor, Dr. Zhongwei Jiang, for his supervision, advice, and guidance from the very early stage of this research as well as giving me extraordinary experiences through out the work. Above all and the most needed, he provided me unflinching encouragement and support in various ways. His truly scientist intuition has made him as a constant oasis of ideas and passions in science, which exceptionally inspire and enrich my growth as a student, a researcher and a scientist want to be. I am indebted to him more than he knows.

I would like to thank all the other members of the committee: Prof.Kanya Tanaka, Prof.Kakuji Ogawara, prof.Xin Chen and Dr.Minoru Morita, for their thoroughly reviewing my thesis, and the valuable comments and suggestions.

I gratefully acknowledge Dr. Haibin Wang for her advice, supervision, and crucial contribution, I am grateful in every possible way and hope to keep up our collaboration in the future.

ÙI would like to thank all of my colleagues in the Micro-mechatronics labora-

tory, especially Dr.Morita, Yu Fang and Ting Tao, for their necessary help during my Ph.D study.

Words fail me to express my appreciation to my wife Chi Cheng whose dedication, love and persistent confidence in me, has taken the load off my shoulder. I owe her for being unselfishly let her intelligence, passions, and ambitions collide with mine. I would like to thank my lovely daughter, Yuran Sun.

Finally, I would like to thank everybody who was important to the successful realization of thesis, as well as expressing my apology that I could not mention personally one by one.

Bibliography

[1] Wikipedia. http://en.wikipedia.org/wiki/Congenital_heart_defect, 2012. 1

[2] MedlinePlus. Congenital heart defect corrective surgeries. http://www.nlm.nih.gov/medlineplus/ency/article/002948.htm, 2012. 1

[3] MedlinePlus. Types of congenital heart defects. http://www.nhlbi.nih.gov/health/health-topics/topics/chd/types.html, 2012. 1

[4] Medicine. Ventricular septal defect(vsd). http://www.medicinenet.com/ventricular_septal_defect/article.htm, july 2012. 1, 2

[5] Merck. Ventricular septal defect (vsd). http://www.merckmanuals.com/professional/pediatric, 2012. 1

[6] Medic. Ventricular septal defect (vsd). http://www.medic8.com/, 2012. 1

[7] WIKIPEDIA. Ventricular septal defect (vsd). http://en.wikipedia.org/wiki/Ventricular_septal_defect, 2012. 1, 2

[8] VSD. Ventricular septal defect (vsd). http://auscultation.com/Human/Heart/VSD/VSD.htm, 2012. 1

[9] VSD. Advanced physical diagnosis learning and teaching at the bedside. http://depts.washington.edu/physdx/heart/demo.html, 2012. 1

[10] KidsHealth. Chd. http://kidshealth.org/parent/medical/heart/chd, 2012. 1

[11] ACHA. A ventricular septal defect (vsd) is a hole in the wall of the heart between the bottom two chambers. http://www.achaheart.org/resources/for-patients/.aspx, 2012. 2

[12] Cota Navin Gupta, Ramaswamy Palaniappan, Sundaram Swaminathan, and Shankar M. Krishnan. Neural network classification of homomorphic segmented heart sounds. Appl. Soft Comput., 7(1):286{297, January 2007. 4

[13] Moussavi ZM Yadollahi A. A robust method for heart sounds localization using lung sounds entropy. IEEETransactionsonBiomedicalEngineering, 53(3):479{502, 2006. 4

[14] Ramon Martinez-Alajarin, Juan; Ruiz-Merino. Efficient method for events detection in phonocardiographic signals. in:R.A.Carmona,G.Linan-Cembrano(Eds.) Proceedings ofSPIE2005,SPIE5839,2005,, pages 398{409, 2005. 4

[15] H. Liang, S. Lukkarinen, and I. Hartimo. Heart sound segmentation algorithm based on heart sound envelogram. In Computers in Cardiology 1997, pages 105 {108, sep 1997. 4

[16] Zeeshan Syed, Daniel Leeds, Dorothy Curtis, and John Guttag. Audio-visual tools for computer-assisted diagnosis of cardiac disorders. 2012 25th IEEE

International Symposium on Computer-Based Medical Systems (CBMS), 0:207{212, 2006. 4, 5, 18

[17] Zhongwei Jiang and Samjin Choi. A cardiac sound characteristic waveform method for in-home heart disorder monitoring with electric stethoscope. Expert Systems with Applications, 31(2):286 { 298, 2006. 4

[18] Zhonghong Yan, Zhongwei Jiang, Ayaho Miyamoto, and Yunlong Wei. The moment segmentation analysis of heart sound pattern. Computer Methods and Programs in Biomedicine, 98(2):140 { 150, 2010. 5, 16, 20, 31, 32

[19] Chung-Hsien Wu, Ching-Wen Lo, and Jhing-Fa Wang. Computer-aided analysis and classification of heart sounds based on neural networks and time analysis. In Acoustics, Speech, and Signal Processing, 1995. ICASSP-95., 1995 International Conference on, volume 5, pages 3455 {3458 vol.5, may 1995. 5, 6, 18

[20] Sanjay R. Bhatikar, Curt DeGroff, and Roop L. Mahajan. A classifier based on the artificial neural network approach for cardiologic auscultation in pediatrics. *Artificial Intelligence in Medicine*, 33(3):251 { 260, 2005. 5, 6, 18

[21] J.M.Hasenkam E.M.Pedersen-P.K.Paulsen H.Nygaard, L.Thuesen. Non-invasive evaluation of aortic valve stenosis by spectral analysis of heart murmurs. in: ProceedingsoftheAnnualInternationalConferenceoftheIEEE, 6:2584{2585, 1992. 5, 6, 18

[22] E. Ilkay I. Turkoglu, A. Arslan. An expert system for diagnosis of the heart

valve diseases. Expert Systems with Applications, 23(3):229{236, 2002. 5, 6, 11, 18

[23] P. Fritzson T.R., N.E. Reed. Heart sound analysis for symptom detection and computer-aided diagnosis. Simulation Modelling Practice and Theory, 12(2):129{146, 2004. 5, 6, 11, 18

[24] E. Ilkay I. Turkoglu, A. Arslan. An intelligent system for diagnosis of the heart valve diseases with wavelet packet neural networks. Computers in Biology and Medicine, 33(4):319{331, 2003. 5, 6, 11, 18

[25] H.Katz M.E.Travel. Usefulness of a new sound spectral averaging technique to distinguish an innocent systolic murmur from that of aortic stenosis. The American Journal of Cardiology, 95(7):902{904, 2005. 5, 18

[26] M.E D.Kim. Assessment of severity of aortic stenosis through time-frequency analysis of murmur. Chest, 124(5):1638{1644, 2003. 5, 18

[27] H.P. Sava, J.T.E. McDonnell, and K.A.A. Fox. Spectral analysis of first and second heart sounds before and after mechanical heart valve implantation. In Engineering in Medicine and Biology Society, 1994. Engineering Advances: New Opportunities for Biomedical Engineers. Proceedings of the 16th Annual International Conference of the IEEE, pages 1280 {1281 vol.2, 1994. 5, 18

[28] A. Iwata, N. Ishii, N. Suzumura, and K. Ikegaya. Algorithm for detecting the first and the second heart sounds by spectral tracking. Medical and Biological Engineering and Computing, 18:19{26, 1980. 5, 18

[29] Huh JM Chang BC Kim SH, Lee HJ. Spectral analysis of heart valve

sound for detection of prosthetic heart valve diseases. YonseiMedicalJournal, 39(4):302 308, 1998. 5, 18

[30] PH.D.; KUMEO TANAKA M.D. ROBERT J. ADOLPH, M.D.; JOHN F. STEPHENS. The clinical value of frequency analysis of the first heart sound in myocardial infarction. Circulation, 41(6):1003 { 1014, 1970. 5, 18

[31] Samjin Choi and Zhongwei Jiang. Cardiac sound murmurs classification with autoregressive spectral analysis and multi-support vector machine technique. Computers in Biology and Medicine, 40(1):8 { 20, 2010. 5, 6, 18, 35, 40

[32] Corinna Cortes and Vladimir Vapnik. Support-vector networks. In Machine Learning, pages 273{297, 1995. 6

[33] Vladimir N. Vapnik. The nature of statistical learning theory. Springer-Verlag New York, Inc., New York, NY, USA, 1995. 6

[34] Mehmet Fatih Akay. Support vector machines combined with feature selection for breast cancer diagnosis. Expert Systems with Applications, 36(2, Part 2):3240 { 3247, 2009. 6, 40, 44

[35] S.S. Mehta and N.S. Lingayat. Svm-based algorithm for recognition of qrs complexes in electrocardiogram. IRBM, 29(5):310 { 317, 2008. 6, 41

[36] Williamn Thornton Bernard Karnath. Auscultation of the heart. september 2002. 8

[37] D. Kumar, R. Carvalho, M. Antunes, R. Gil, J. Henriques, and L. Eugenio. A new algorithm for detection of s1 and s2 heart sounds. In Acoustics,

Speech and Signal Processing, 2006. ICASSP 2006 Proceedings. 2006 IEEE International Conference on, volume 2, page II, may 2006. 8, 20

[38] Heart sound feature parameters distribution and support vector machine-based classification boundary determination method for ventricular septal defect auscultation. Journal of Computational Science and Technology, 6, 2012. 11, 48

[39] Y. Ozbay R.Ceylan. Comparison of fcm, pca and wt techniques for classification ecg arrhythmias using artificial neural network. Expert Systems with Applications, 33(2):286{295, 2007. 11

[40] M. Fang S.-H. Lai. A hierarchical neural network algorithm for robust and automatic windowing of mr images. *Artificial Intelligence in Medicine*, 19(2):97{119, 2000. 11

[41] A. Alonso-Betanzos V. Moret-Bonillo O. Fontenla-Romero, B. Guijarro-Berdinas. A new method for sleep apnea classification using wavelets and feedforward neural networks. *Artificial Intelligence in Medicine*, 34(1):65{67, 2005. 11

[42] A. Subasi. Usefulness of a new sound spectral averaging technique to distinguish an innocent systolic murmur from that of aortic stenosis. The American Journal of Cardiology, 95(7):902{904, 2005. 11

[43] E.M.G. Olsson B. von Scheele N. Xiong M. Nilsson, P. Funk. Clinical decision-support for diagnosing stress-related disorders by applying psychophysiological medical knowledge to an instance-based learning system. *Artificial Intelligence in Medicine*, 36(2):159{176, 2006. 11, 13

[44] D.A. Linkens J.E. Peacock C.S. Nunes, M. Mahfouf. Modelling and multivariable control in anaesthesia using neural-fuzzy paradigms: part i. classification of depth of anaesthesia and development of a patient model. *Artificial* Intelligence in Medicine, 35(3):195{206, 2005. 11

[45] Wavelets W. Sweldens. what next. Proceedings of the IEEE 84, 1996, page 680?685, 1996. 12

[46] H. Guo C.S. Burrus, R.A. Gopinath. Introduction to Wavelets and Wavelet Transforms. Prentice-Hall, New Jersey, 1998. 12, 13

[47] A.K. Chan J.C. Goswami. Fundamentals of Wavelets?Theory, Algorithms, and Applications. Wiley, New York, 1999. 12, 13

[48] S.G. Mallat. A Wavelet Tour of Signal Processing. Academic Press, San Diego, 1999. 12, 13

[49] I. Daubechies. Orthogonal bases of compactly supported wavelets. Communications on Pure and Applied Mathematics, 41(7):909{996, 1988. 13

[50] Zhongwei Jiang and Samjin Choi. A cardiac sound characteristic waveform method for in-home heart disorder monitoring with electric stethoscope. Expert Systems with Applications, 31(2):286 { 298, 2006. 16, 17, 19, 20, 35

[51] Zhongwei Jiang Samjin Choi. Development of wireless heart sound acquisition system for screening heart valvular disorder. Proceedings of the International Conference on Instrumentation, Control and Information Technology(SICE), pages 3771{3776, 2005. 16, 20

[52] D. Kumar, R. Carvalho, M. Antunes, R. Gil, J. Henriques, and L. Eugenio. A new algorithm for detection of s1 and s2 heart sounds. In Acoustics, Speech and Signal Processing, 2006. ICASSP 2006 Proceedings. 2006 IEEE International Conference on, volume 2, page II, may 2006. 17

[53] M.B. Malarvili, I. Kamarulafizam, S. Hussain, and D. Helmi. Heart sound segmentation algorithm based on instantaneous energy of electrocardiogram. In Computers in Cardiology, 2003, pages 327 { 330, sept. 2003. 19

[54] A. Haghighi-Mood and J.N Torry. A sub-band energy tracking algorithm for heart sound segmentation. Computers in Cardiology, pages 501 {504, sept 1995. 19

[55] D. Kumar, P. Carvalho, M. Antunes, J. Henriques, M. Maldonado, R. Schmidt, and J Habetha. Wavelet transform and simplicity based heart murmur segmentation. Computers in Cardiology, pages 173 {176, 2006. 20

[56] Liang Huiying, L. Sakari, and H Iiro. A heart sound segmentation algorithm using wavelet decomposition and reconstruction. Engineering in Medicine and Biology Society, 1997. Proceedings of the 19th Annual International Conference of the IEEE, 4:1630 {1633, oct 1997. 20

[57] S. Omran and M Tayel. A heart sound segmentation and feature extraction algorithm using wavelets. Control, Communications and Signal Processing, 2004, pages 235 { 238, 2004. 20

[58] Samjin Choi and Zhongwei Jiang. Comparison of envelope extraction algorithms for cardiac sound signal segmentation. Expert Systems with Applications, 34(2):1056 { 1069, 2008. 20

[59] G.M. Livadas and A.G. Constantinides. Image edge detection and segmentation based on the hilbert transform. In Acoustics, Speech, and Signal Processing, 1988. ICASSP-88., 1988 International Conference on, pages 1152 {1155 vol.2, apr 1988. 22

[60] Klaus Kohlmann. Corner detection in natural images based on the 2-d hilbert transform. Signal Processing, 48(3):225 { 234, 1996. 22

[61] Woo-Hyuk Jung and Sang-Goog Lee. An r-peak detection method that uses an svd filter and a search back system. Computer Methods and Programs in Biomedicine, (0):{, 2012. 22

[62] HeartRate. Heart rate chart. http://www.heart.com/heart-rate-chart.html, Dec 2012. 30

[63] Enotes. Cardiac cycle. http://www.enotes.com/cardiac-cycle-reference, july 2012. 30

[64] University of Michigan. Heart sound and murmur library. http://www.med.umich.edu/lrc/psb/heartsounds/index.htm, july 2012. 30

[65] V. N. Vapnik. An overview of statistical learning theory. IEEE, 10(5):988{999, 1999. 40

[66] D.P. Bertsekas. Nonlinear programming. Optimization and neural computation series. Athena Scientific, 1995. 42

[67] R. Courant and D. Hilbert. Methods of mathematical physics. Number 1 in Wiley classics library. Wiley, 1989. 42

[68] Walter Gander, GeneH. Golub, and Rolf Strebel. Least-squares fitting of circles and ellipses. BIT Numerical Mathematics, 34:558{578, 1994. 51

[69] Kieran F. Mulchrone and Kingshuk Roy Choudhury. Fitting an ellipse to an arbitrary shape: implications for strain analysis. Journal of Structural Geology, 26(1):143 { 153, 2004. 51

[70] T.J. Wynn and S.A. Stewart. Comparative testing of ellipse-fitting algorithms: implications for analysis of strain and curvature. Journal of Structural Geology, 27(11):1973 { 1985, 2005. 51

[71] Anandaroop Ray and Deepak C. Srivastava. Non-linear least squares ellipse fitting using the genetic algorithm with applications to strain analysis. Journal of Structural Geology, 30(12):1593 { 1602, 2008. 51

[72] Xiangzhi Bai, Changming Sun, and Fugen Zhou. Splitting touching cells based on concave points and ellipse fitting. Pattern Recognition, 42(11):2434 { 2446, 2009. 51

[73] D. Chaudhuri. A simple least squares method for fitting of ellipses and circles depends on border points of a two-tone image and their 3-d extensions. Pattern Recognition Letters, 31(9):818 { 829, 2010. 51

[74] Kenichi Kanatani and Prasanna Rangarajan. Hyper least squares fitting of circles and ellipses. Computational Statistics & Data Analysis, 55(6):2197 { 2208, 2011. 51

[75] Dilip K. Prasad, Maylor K.H. Leung, and Chai Quek. Ellifit: An uncon-

strained, non-iterative, least squares based geometric ellipse fitting method. Pattern Recognition, (0):{, 2012. 51

[76] Sung Joon Ahn, Wolfgang Rauh, and Hans-Jrgen Warnecke. Least-squares orthogonal distances fitting of circle, sphere, ellipse, hyperbola, and parabola. Pattern Recognition, 34(12):2283 { 2303, 2001. 51

[77] K. Higuchi, K. Sato, H. Makuuchi, A. Furuse, S. Takamoto, and H. Takeda. Automated diagnosis of heart disease in patients with heart murmurs: application of a neural network technique. J Med Eng Technol, 30(2):61 { 68, 2006. 65